Since January 2020 Elsevier has created a COVID-19 resource centre with free information in English and Mandarin on the novel coronavirus COVID-19. The COVID-19 resource centre is hosted on Elsevier Connect, the company's public news and information website.

Cell

Article

TOP1 inhibition therapy protects against SARS-CoV-2-induced lethal inflammation

Graphical abstract

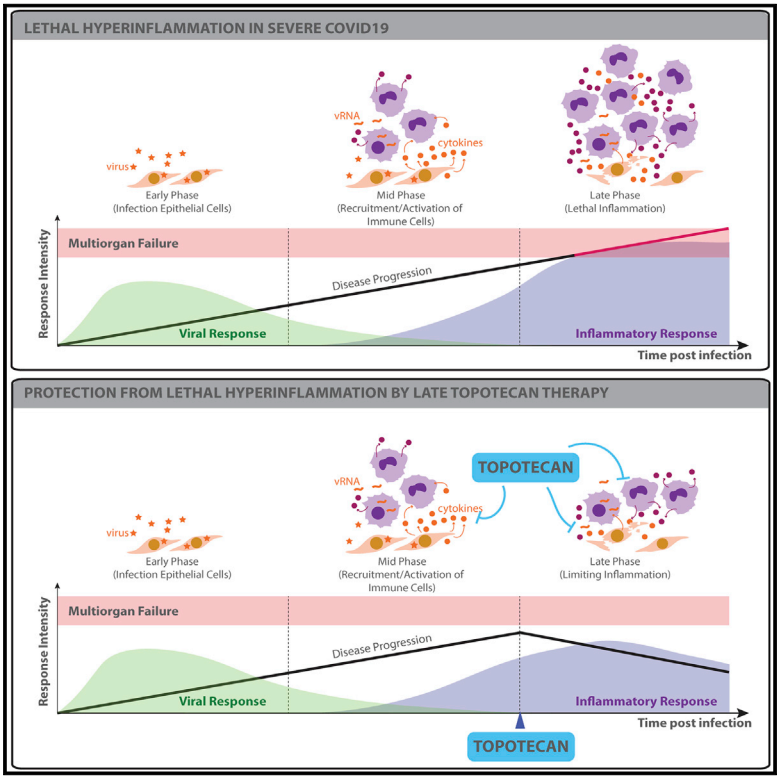

Highlights

- TOP1 activates inflammatory gene expression during SARS-CoV-2 infection
- Topotecan (TPT), a TOP1 FDA-approved drug, suppresses inflammatory gene expression
- Inflammatory genes suppressed by TPT are overexpressed in COVID-19 lung autopsies
- TPT therapy protects from hyper-inflammation and death in preclinical models

Authors

Jessica Sook Yuin Ho, Bobo Wing-Yee Mok, Laura Campisi, ..., Christopher Benner, Juergen A. Richt, Ivan Marazzi

Correspondence

ivan.marazzi@mssm.edu

In brief

Inhibition of topoisomerase 1 through the FDA-approved molecule topotecan suppresses SARS-CoV-2-infection-associated lethal inflammation in hamster and mouse models without compromising antiviral immune responses.

Ho et al., 2021, Cell *184*, 2618–2632
May 13, 2021
https://doi.org/10.1016/j.cell.2021.03.051

CellPress

CellPress

Cell

Article

TOP1 inhibition therapy protects against SARS-CoV-2-induced lethal inflammation

Jessica Sook Yuin Ho,[1,31] Bobo Wing-Yee Mok,[2,31] Laura Campisi,[1] Tristan Jordan,[1] Soner Yildiz,[1] Sreeja Parameswaran,[4] Joseph A. Wayman,[9,27] Natasha N. Gaudreault,[10] David A. Meekins,[10] Sabarish V. Indran,[10] Igor Morozov,[10] Jessie D. Trujillo,[10] Yesai S. Fstkchyan,[1] Raveen Rathnasinghe,[1] Zeyu Zhu,[1] Simin Zheng,[1] Nan Zhao,[1] Kris White,[1] Helen Ray-Jones,[3] Valeriya Malysheva,[3] Michiel J. Thiecke,[26] Siu-Ying Lau,[2] Honglian Liu,[2] Anna Junxia Zhang,[2] Andrew Chak-Yiu Lee,[2] Wen-Chun Liu,[1] Sonia Jangra,[1] Alba Escalera,[1] Teresa Aydillo,[1] Betsaida Salom Melo,[12,13] Ernesto Guccione,[11] Robert Sebra,[12,13,29,30] Elaine Shum,[5] Jan Bakker,[14,15,16] David A. Kaufman,[17] Andre L. Moreira,[18]

(Author list continued on next page)

[1]Department of Microbiology, Icahn School of Medicine at Mount Sinai, New York, NY 10029, USA
[2]Department of Microbiology and State Key Laboratory for Emerging Infectious Diseases, Li Ka Shing Faculty of Medicine (HKUMed), The University of Hong Kong, Hong Kong
[3]MRC London Institute of Medical Sciences, London W12 0NN, UK
[4]Center for Autoimmune Genomics and Etiology, Cincinnati Children's Hospital Medical Center, Cincinnati, OH 45229, USA
[5]Division of Medical Oncology and Hematology, NYU Langone Perlmutter Cancer Center, New York, NY 10016, USA
[6]Department of Haematology-Oncology, National University Hospital and Cancer Science Institute of Singapore, National University of Singapore, 117599 Singapore, Singapore
[7]Department of Medicine, School of Medicine, University of California, San Diego, La Jolla, CA 92092, USA
[8]Center of Excellence for Emerging and Zoonotic Animal Diseases (CEEZAD), Kansas State University, Manhattan, KS, USA
[9]Divisions of Immunobiology and Biomedical Informatics, Cincinnati Children's Hospital, Cincinnati, OH 45229, USA
[10]Diagnostic Medicine and Pathobiology, College of Veterinary Medicine, Kansas State University, 1800 Denison Avenue, Manhattan, KS 66506, USA
[11]Tisch Cancer Institute, Department of Oncological Sciences and Department of Pharmacological Sciences, Icahn School of Medicine at Mount Sinai, New York, NY, USA
[12]Department of Genetics and Genomics, Icahn School of Medicine at Mount Sinai, New York, NY, USA
[13]Icahn Institute of Genomics and Multiscale Biology, Icahn School of Medicine at Mount Sinai, New York, NY, USA
[14]Pontificia Universidad Católica de Chile, Santiago, Chile
[15]Erasmus MC University Medical Center Rotterdam, Rotterdam, the Netherlands
[16]Editor in Chief, Journal of Critical Care, NYU School of Medicine, Columbia University College of Physicians & Surgeons, New York, NY, USA

(Affiliations continued on next page)

SUMMARY

The ongoing pandemic caused by severe acute respiratory syndrome coronavirus 2 (SARS-CoV-2) is currently affecting millions of lives worldwide. Large retrospective studies indicate that an elevated level of inflammatory cytokines and pro-inflammatory factors are associated with both increased disease severity and mortality. Here, using multidimensional epigenetic, transcriptional, *in vitro*, and *in vivo* analyses, we report that topoisomerase 1 (TOP1) inhibition suppresses lethal inflammation induced by SARS-CoV-2. Therapeutic treatment with two doses of topotecan (TPT), an FDA-approved TOP1 inhibitor, suppresses infection-induced inflammation in hamsters. TPT treatment as late as 4 days post-infection reduces morbidity and rescues mortality in a transgenic mouse model. These results support the potential of TOP1 inhibition as an effective host-directed therapy against severe SARS-CoV-2 infection. TPT and its derivatives are inexpensive clinical-grade inhibitors available in most countries. Clinical trials are needed to evaluate the efficacy of repurposing TOP1 inhibitors for severe coronavirus disease 2019 (COVID-19) in humans.

INTRODUCTION

The ongoing coronavirus disease 2019 (COVID-19) pandemic caused by severe acute respiratory syndrome coronavirus 2 (SARS-CoV-2) has affected millions of lives worldwide and poses an overwhelming burden on global health systems and economy. The development of novel therapeutics against SARS-CoV-2 remains a top priority. While prophylactic

CellPress

Mariano Carossino,[19] Udeni B.R. Balasuriya,[19] Minji Byun,[20] Randy A. Albrecht,[1,21] Michael Schotsaert,[1,21] Adolfo Garcia-Sastre,[1,11,21,22] Sumit K. Chanda,[23] Emily R. Miraldi,[9,27] Anand D. Jeyasekharan,[6] Benjamin R. TenOever,[1,21,24] Mikhail Spivakov,[3] Matthew T. Weirauch,[4,25,28] Sven Heinz,[7] Honglin Chen,[2] Christopher Benner,[7] Juergen A. Richt,[8,10] and Ivan Marazzi[1,21,32,*]

[17]Division of Pulmonary, Critical Care, and Sleep Medicine, Department of Medicine, NYU School of Medicine, New York, NY, USA
[18]Department of Pathology, New York University School of Medicine, New York, NY, USA
[19]Louisiana Animal Disease Diagnostic Laboratory and Department of Pathobiological Sciences, School of Veterinary Medicine, Louisiana State University, Baton Rouge, LA, USA
[20]Department of Medicine, Clinical Immunology, Icahn School of Medicine at Mount Sinai, New York, NY, USA
[21]Global Health and Emerging Pathogens Institute, Icahn School of Medicine at Mount Sinai, New York, NY, USA
[22]Department of Medicine, Division of Infectious Diseases, Icahn School of Medicine at Mount Sinai, One Gustave L. Levy Place, Box 1124, New York, NY 10029, USA
[23]Immunity and Pathogenesis Program, Infectious and Inflammatory Disease Center, Sanford Burnham Prebys Medical Discovery Institute, La Jolla, CA 92037, USA
[24]Virus Engineering Center for Therapeutics and Research, Icahn School of Medicine at Mount Sinai, New York, NY, USA
[25]Department of Pediatrics, University of Cincinnati, College of Medicine, Cincinnati, OH 45229, USA
[26]Enhanc3D Genomics Ltd, Cambridge CB22 0AT, UK
[27]Department of Pediatrics, University of Cincinnati, College of Medicine, Cincinnati, OH 45229, USA
[28]Divisions of Biomedical Informatics and Developmental Biology, Cincinnati Children's Hospital Medical Center, Cincinnati, OH 45229, USA
[29]Sema4, a Mount Sinai venture, Stamford, CT, USA
[30]Black Family Stem Cell Institute, Icahn School of Medicine at Mount Sinai, New York, NY 10029, USA
[31]These authors contributed equally
[32]Lead contact
*Correspondence: ivan.marazzi@mssm.edu
https://doi.org/10.1016/j.cell.2021.03.051

measures are being evaluated and distributed, drugs available to target SARS-CoV-2 and function therapeutically are direly needed, especially for severe cases of COVID-19.

Disease progression in severe COVID-19 features an initial phase of increasing viremia that wears off and is followed by a second phase characterized by a steep increase in systemic inflammation (Lee et al., 2020; Merad and Martin, 2020; Siddiqi and Mehra, 2020).

Several studies have shown that levels of inflammatory molecules can help distinguish those who survive COVID-19 from those who do not. For example, increased levels of interleukin-6 (IL-6) and fibrin degradation products (D-dimer), as well as other single measurements like C-reactive protein (CRP) or combined-measurement parameters (Sequential Organ Failure Assessment; SOFA score), have been correlated with risk for death from COVID-19. (Zhou et al., 2020a). Notably, all non-survivors experienced sepsis (Zhou et al., 2020a). Therefore, the increased systemic inflammation that occurs during disease progression provides a biological rationale for interrupting hyper-inflammation to reduce disease severity. Guided by this logic, clinical trials have begun to examine the efficacy of cytokine blockers and anti-inflammatory molecules as potential COVID-19 therapeutics (Merad and Martin, 2020).

However, inhibition of single cytokines such as interleukin 6 (IL-6) or granulocyte-macrophage colony-stimulating factor (GM-CSF) might not be sufficient (Hermine et al., 2021; Salvarani et al., 2021). This is due to the fact that many signaling molecules and pathways are involved in triggering an inflammatory response. Additionally, levels of individual cytokines can vary depending on the age and the clinical history of the patient, thus limiting the scope of therapeutics that only target a single inflammatory molecule.

Infection causes a rapid and orchestrated gene induction governed by expression of antiviral and inflammatory mediators. This is often referred to as "infection-induced gene program." In many instances, the magnitude of induction of the inflammatory components in a gene program can be overwhelming and become more harmful than protective. Such overt induction of inflammatory genes can be driven by unique features of the infectious agent. For example, viral antagonism in infected cells may delay initial responses, causing inappropriate and prolonged production of pro-inflammatory genes and immunopathology later in infection (Channappanavar et al., 2016; Channappanavar and Perlman, 2017). Alternatively, excessive inflammation may be immune mediated and driven by excessive local or systemic recruitment and activation of immune cells. The ultimate result is an overt expression of inflammatory mediators that is fatal to the host.

Reducing the magnitude of the induction of gene expression upon infection might hold the key to the development of novel therapeutics for infections associated with hyper-inflammation. Previously, we reported that chromatin factors play key roles in controlling the induction of inflammatory gene expression programs (Marazzi et al., 2012; Miller et al., 2015; Nicodeme et al., 2010). Targeting the activity of these proteins acting on the chromatin template, where infection-induced gene transcription is executed, leads to partial suppression (buffering) of multiple genes (Marazzi et al., 2012; Miller et al., 2015; Nicodeme et al., 2010). Such simultaneous inhibition of many virus-induced genes "in one go" can have a clear advantage over conventional single target therapies (Marazzi et al., 2018).

In fact, there are at least two scenarios in which reducing the induction of gene expression upon infection could be advantageous. In the first scenario, partial suppression of infection-induced antiviral and inflammatory genes in the cells targeted by virus results in retaining an amount of antiviral molecules for blocking viral replication while avoiding

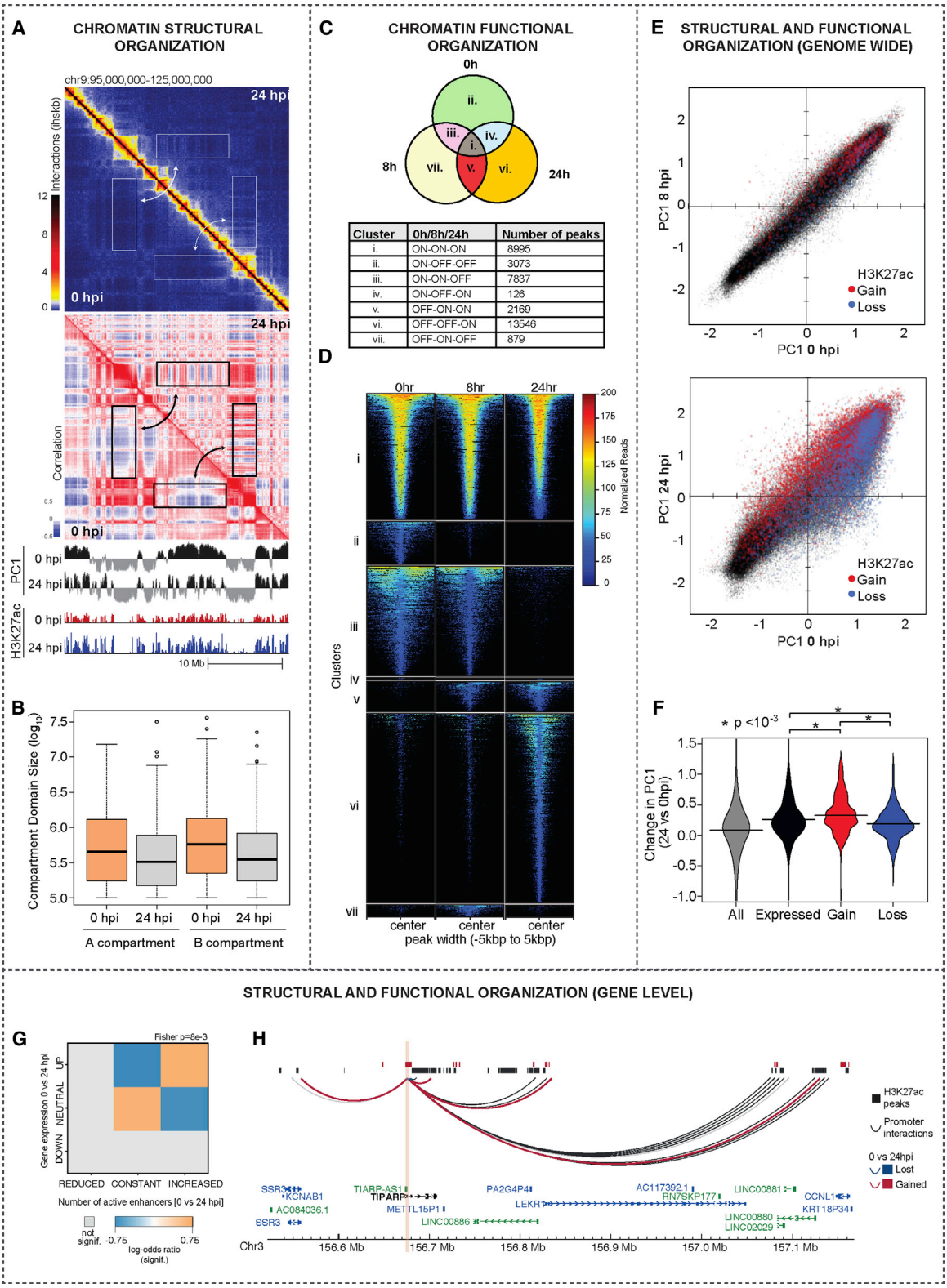

Figure 1. SARS-CoV-2 restructures chromatin in host cells

(A) Top: normalized Hi-C contact matrices are shown for the uninfected (0 hpi) control (lower left) and 24 h post-infection (hpi; upper-right) for a representative 30-Mb region of chromosome 9. White rectangles highlight regions with strong changes in interaction patterns between conditions. Middle: pairwise correlation

(legend continued on next page)

excessive induction of inflammatory genes and pathways. A second scenario is when the gene programs are triggered by noninfected immune cells that respond to pathogen-associated molecular patterns (PAMPs) or damage-associated molecular patterns (DAMPs) in an overwhelmingly inflammatory fashion. This latter scenario occurs in many instances of infection that leads to sepsis.

We have previously shown that the host enzyme topoisomerase 1 (TOP1) is required to fully transactivate infection-induced genes and thus controls the establishment of inflammatory gene programs during many viral and bacterial infection and co-infections (Rialdi et al., 2016). Therapeutic administration (after infection) of one to three doses of topoisomerase inhibitors can rescue mortality in four animal models of inflammation-induced death (Rialdi et al., 2016). These data support the hypothesis that host-directed epigenetic therapy can suppress hyper-inflammatory responses upon infection without compromising pathogen clearance. At that time (2016), we also predicted that this strategy could be useful for future pandemics. We present here a series of experiments in which we tested the hypothesis that modifying the host response to SARS-CoV-2 infection with epigenetic therapy can ameliorate severe COVID-19.

RESULTS

Cell signaling cascades converge on chromatin to dictate changes in gene expression upon cell-intrinsic and extrinsic signals. Gene expression programs are controlled by transcriptional activity, which is, in turn, influenced by changes in chromatin structural (physical movement of genes into chromatin compartments or enhancer-promoter interaction) and functional (epigenetic modifications that demarcate regions of gene activity) organization.

Comparison between how a signal is received and decoded at the chromatin level and the final output of gene expression can elucidate how a pathogen alters the host gene expression program during infection. More importantly, it can instruct the targeting of chromatin factors in order to achieve a partial suppression (buffering) of infection-induced gene expression programs.

In an effort to understand how SARS-CoV-2 alters chromatin function and gene activity upon infection, we performed a combined structural and epigenetic analysis during infection.

To first characterize structural chromatin changes, we performed Hi-C on uninfected and SARS-CoV-2-infected A549 cells expressing the human SARS-CoV-2 entry receptor angiotensin-I-converting enzyme 2 (ACE2) (A549-ACE2) at both early (8 h) and late (24 h) time points post-infection. Reproducible results were achieved across replicates for all time points (Table S1). Our analysis indicates that large portions of the genome alter their global interaction profiles as infection progresses, culminating in a major redistribution of chromatin associated with either the active (A) or inactive (B) compartments at the 24-h time point (Figure 1A).

Notably, compartment changes result in a shortening of the domain size, with large linear stretches of A and B compartment chromatin generally becoming divided into A/B subdomains (Figures 1A and 1B). To determine whether these topological effects are unique to SARS-CoV-2, we performed temporal Hi-C profile during infection by influenza A virus (IAV). Our results indicate that similar to SARS-CoV-2 infection, influenza virus infection causes A-B and B-A changes and domain shortening at later time points post-infection (Figures S1A and S1B). These results indicate that chromosomal compartmentalization is affected by infection-induced signals, suggesting that large chromatin domains (megabases) lose structural constraints imposed by cohesin (Rao et al., 2017; Schwarzer et al., 2017),

While the resolution limit of Hi-C does not allow to us characterize single genes in A and B domains, we could still determine if the large-scale structural changes were associated with functional changes to chromatin organization and transcriptional activity. To do this, we performed chromatin immunoprecipitation sequencing (ChIP-seq) for histone 3 lysine 27 acetylation (K27ac), an epigenetic mark found at active regulatory regions (promoters and enhancers) that is commonly used to monitor dynamic changes in transcriptional activation. ChIP-seq for K27ac was performed in uninfected and infected A549-ACE2 cells at both early (8 h) and late (24 h) time points post-infection. Our analysis showed high correlation of K27ac levels between replicates (Figure S1C). While some regions of the genome showed

matrices for uninfected control and 24 hpi Hi-C experiments analysis for the same region shown in the upper panel. Bottom: PC1 values are shown along with H3K27ac ChIP-seq levels for the region depicted.

(B) Distribution of A and B compartment domain sizes genome wide for uninfected control and 24 hpi A549-ACE2 cells.

(C) Venn diagram schematic depicting the seven possible patterns of peak occurrence (i–vii), along with the number of peaks observed for each pattern at 0, 8, and 24 hpi. ON/OFF indicates the presence or absence of peaks, respectively.

(D) Differential H3K27ac across infection time points. H3K27ac ChIP-seq peaks were classified across the infection time course into clusters by their pattern of occurrence. Heatmap indicates the normalized H3K27ac read count intensity within each unique peak (rows) for each of the three time points (columns; 0, 8, and 24 h), for the clusters (i–vii) described in (C).

(E) Scatterplot comparing the PC1 values for every 25-kb region in the genome for uninfected control and infected cells (8 and 24 hpi). Data points colored red or blue indicate that they overlap with a significantly regulated H3K27ac peaks (4-fold, adjusted p value < 0.05).

(F) Distribution of the change in PC1 values between uninfected and 24 hpi at the promoters of genes that are either expressed in A549-Ace2 cells, induced, or repressed by SARS-CoV-2 infection (>1.5-fold, adjusted p value < 0.05).

(G) Gene expression dynamics and changes in the number of connected active enhancers presented as a heatmap of log-odds ratios. Both interaction rewiring and changes in K27ac at PIRs is taken into account.

(H) Dynamics of promoter interactions and enhancer activity (proxied by K27ac) between 0 and 24 hpi for the *TIPARP* gene (upregulated upon infection). K27ac peaks gained at 24 hpi are highlighted in dark red (log_2 fold change [LFC] > 2, padj < 0.05). Lost (blue) and gained (dark red) promoter interactions with K27ac regions ("enhancers") at 24 hpi are shown as colored arcs and the rest shown in black. Light-gray arcs represent interactions with regions without K27ac detected at any time point.

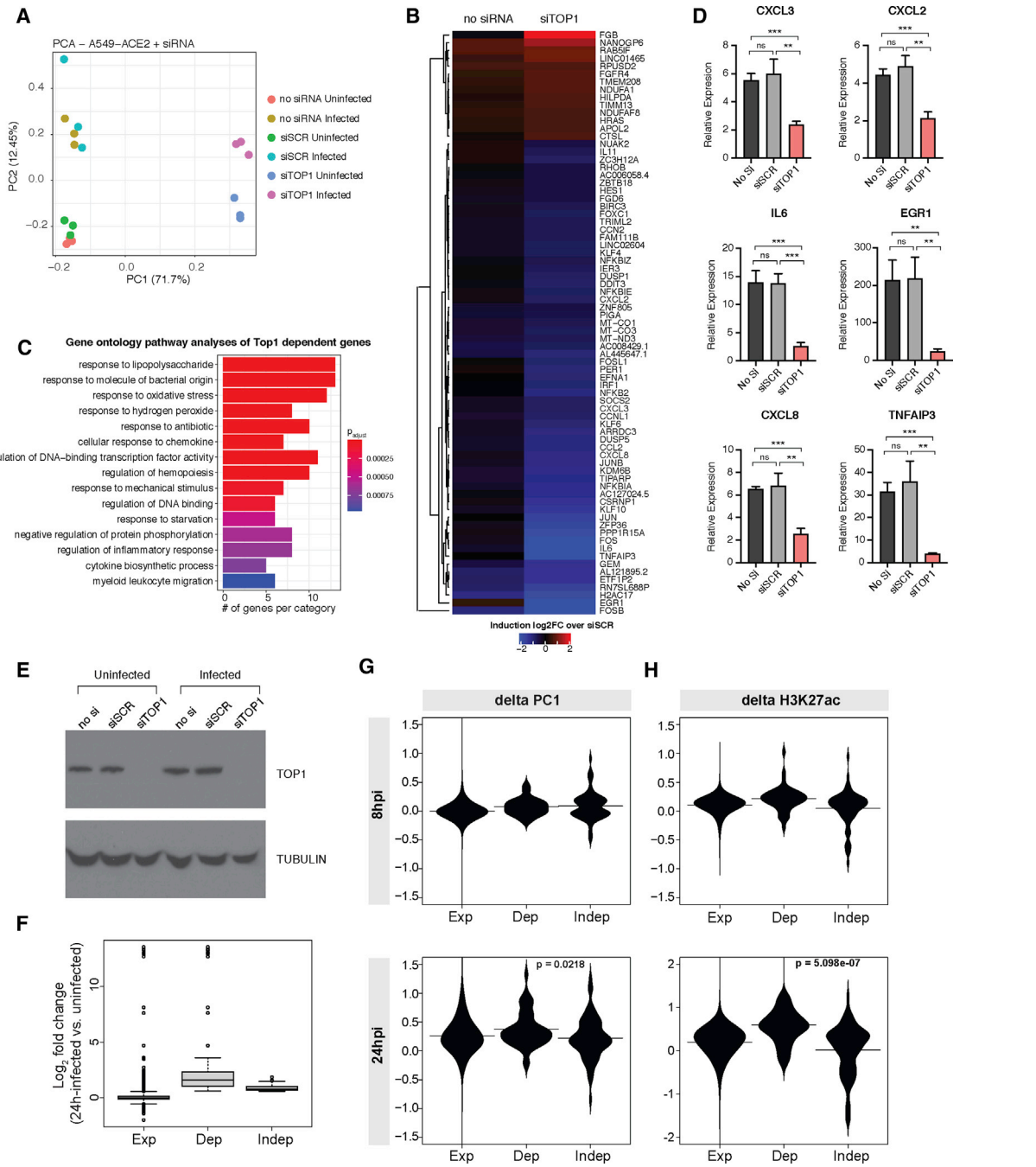

Figure 2. TOP1 depletion in SARS-CoV-2 infected cells inhibits induction of inflammatory genes

(A) PCA plot showing the relationship between samples, replicates, and treatment conditions.

(B) Heatmap showing relative changes in gene expression levels in no siRNA (no siRNA) or siTOP1 (siTOP1)-treated cells when compared to nontargeting control siRNA-treated (siSCR) cells. Shown are genes that are differentially expressed between siTOP1 and siSCR samples (adjusted p value < 0.05, fold change > 1.5).

(C) Gene Ontology analyses of downregulated target genes shown in (B).

(D) qPCR validation of select target genes shown in (B). Shown are the mean and SD of three replicates. *p < 0.05; **p < 0.01; ***p < 0.005, ****p < 0.001 by two-tailed, unpaired Students' t test. Data are plotted relative to the corresponding uninfected controls.

(E) Western blot showing TOP1 and tubulin levels in no siRNA (no si), control siRNA (siSCR)-, or TOP1 siRNA (siTOP1)-treated uninfected and infected cells. Shown is a representative western blot of three independent experiments.

(F) Boxplots showing changes in gene expression levels upon SARS-CoV-2 infection, as quantified by RNA-seq, for all expressed genes (Exp), TOP1-dependent induced genes (Dep), and TOP1-independent induced genes (Indep).

(legend continued on next page)

no change in K27ac levels upon infection (cluster i), there were significant changes in K27ac levels at promoters and other regulatory regions during the course of infection (clusters ii–vii; Figure 1C; Tables S2A–S2C). Regions that significantly gain (clusters v and vi; Figure 1C) and lose K27ac (clusters ii and iii; Figure 1C) over the course of infection were detected.

We then combined structural and functional information by overlaying the changes in K27ac and DNA topology. Our analysis indicates that regions that gain or lose K27ac are enriched in chromatin domains that move from B-A (inactive to active) or A-B (active to inactive) compartments, respectively (Figure 1E). This partitioning occurs dynamically throughout infection (Figure 1E; compare 8 h versus 24 h) and is associated with gene expression activity (Figure 1F). These results suggest that the dynamic restructuring of genome compartmentalization by SARS-CoV-2 infection is highly associated with transcriptional activity.

To characterize whether a unique set of transcription factors might drive these changes, we performed motif enrichment analysis of regions displaying differential H3K27ac activity. Our results indicate that repressed regions lack unique enrichment of immune-specific transcription factors at promoters, enhancers, and other putative regulatory regions (Figure S1D; Table S2D). Regions that gain K27ac signal display a strong enrichment for motifs recognized by nuclear factor κB (NF-κB) (red bars), AP1 (orange bars), and to a lesser extent interferon regulatory factor (IRF) and signal transducer and activator of transcription (STAT) transcription factors (green and blue bars respectively, clusters v and vi; Figure S1D; Table S2D). These data suggest that the epigenetic landscape established as a result of the infection (and viral antagonism) is skewed toward the usage of regulatory regions controlling inflammatory responses

To then provide direct evidence that identified regulatory regions do indeed contact a given gene promoters to sustain gene transactivation, we performed promoter capture Hi-C. This technique measures enhancer-promoter interactions at a single-gene resolution. Promoter capture Hi-C was conducted in SARS-CoV-2-infected A549-ACE2 cells at 8 and 24 hpi, as well as in uninfected cells (0 hpi). Following alignment and quality control, we detected a total of 63,804 interactions between 11,244 promoters and 40,387 promoter-interacting regions (PIRs) across the three time points using CHiCAGO (Cairns et al., 2016). Based on unsupervised clustering and post hoc filtering, we classified the promoter interactions into three broad categories based on their dynamics upon infection: 10,983 "lost," 11,022 "retained," and 11,334 "gained" (see STAR Methods for details).

To obtain a gene-level view, we computed the change in the number of active enhancers connected to each gene between 0 and 24 hpi, accounting for promoter interaction rewiring and changes in enhancer activity at the PIRs of either preexisting or novel contacts. We found a significant association between this property and gene expression dynamics (Figure 1G; Fisher's test $p = 0.008$). In particular, an increase in the number of promoter-connected active enhancers associated with upregulation of their respective target genes (Figure 1G; log-odds ratio [LOR] = 0.74; 95% confidence interval [CI], 0.13–1.30). Examples of the detected promoter interaction profiles at each time point for *TIPARP* and *NFKIBIZ* genes that are strongly induced upon infection (log2 fold change [log2FC] > 1) are shown in Figures 1H and S1E, respectively.

Overall, our results characterized the epithelial cell gene expression programs upon infection with respect to global topological effects, as well as local topological and epigenetic changes that dictate enhancer-promoter rewiring and gene activity. Our results indicate that because of infection-induced epigenetic remodeling and the effect of viral antagonism geared to suppress antiviral responses (Banerjee et al., 2020b; Lei et al., 2020), infection induces genes that are mostly inflammatory. These genes are regulated by specific repertoire of transcription factors and display prototypical epigenetic features of transactivation, suggesting that unique host chromatin factors dictate the magnitude of their transcriptional induction.

TOP1 controls SARS-CoV-2-induced gene expression response

To determine whether chromatin factors can control the transactivation of SARS-CoV-2-induced genes, we focused our attention on TOP1, a factor known to activate bacterial- and viral-infection-induced genes (Rialdi et al., 2016). We performed small interfering RNA (siRNA)-mediated knockdown of TOP1 (siTOP1) along with control siRNA (siSCR) in A549-ACE2 cells, followed by mock treatment (PBS only; uninfected controls) or infection with SARS-CoV-2. Gene expression changes in these cells were quantified by RNA sequencing (RNA-seq) at 24 h post-infection (hpi). Our analyses indicate that siTOP1 treated cells had a distinct transcriptional response to the virus (Figure 2A) as compared to no siRNA or siSCR-treated cells, resulting in selective suppression of many infection-induced genes (fold change > 1.5, adjusted p value [padj] < 0.05; Figures 2B and 2C; Tables S3 . Gene Ontology (GO) pathway analyses of genes that are downregulated upon TOP1 knockdown suggest that many of these genes are involved in inflammatory responses (Figure 2C; Table S3C). We further validated our results by qPCR for representative genes IL-6, CXCL2, CXCL3, CXCL8, EGR1, and TNFAIP3 (Figure 2D), verifying that depletion of TOP1 protein levels (Figure 2E) reduces the expression of these inflammatory genes.

To understand the specificity of TOP1, we profiled infection-induced and TOP1 dependent genes ("Dep."; Table S3D) identified in Figure 2B with respect to their structural and epigenetic status at basal state and after infection. As controls, we used all expressed genes ("Exp"; Table S3D) or genes that are also induced by infection but unaffected by TOP1 depletion (TOP1 independent, "Indep."; Table S3D). Our analysis indicates that genes that depend on TOP1 for their upregulation are induced to higher levels then TOP1-independent genes upon infection (Figure 2F). TOP1-dependent genes also displayed greater shifts toward active chromatin compartment (positive delta PC1 levels;

(G) Violin plots showing changes in PC1 (delta PC1) at 8 and 24 hpi at expressed genes (Exp), TOP1-dependent induced genes (Dep), and TOP1-independent induced genes (Indep). Horizontal lines indicate the means.
(H) Violin plots showing changes in H3K27ac levels (delta H3K27ac) for 8 and 24 hpi at expressed genes (Exp), TOP1-dependent induced genes (Dep), and TOP1-independent induced genes (Indep). Horizontal lines indicate the means.

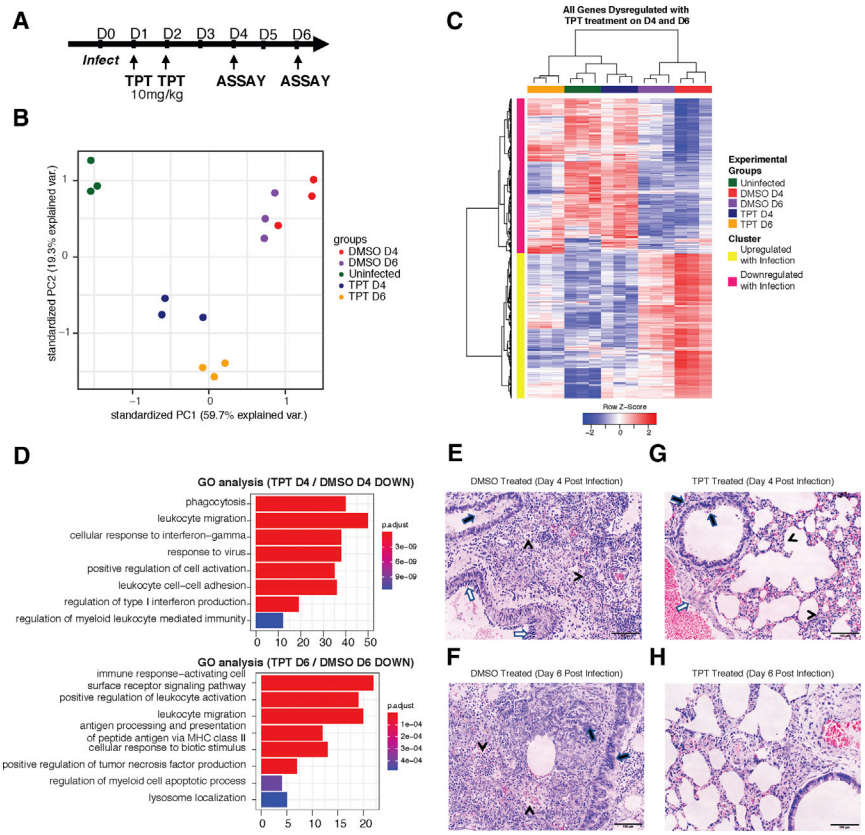

Figure 3. TPT treatment reduces inflammatory gene expression in SARS-CoV-2 infected hamsters

(A) Schematic showing the infection and treatment regime used.

(B) PCA plot showing the relationship between treatment and infection groups.

(C) Heatmap showing gene expression levels of genes that are dysregulated with TPT treatment in uninfected (green), DMSO- (red and purple), or TPT-treated (blue and yellow) hamsters at days 4 and 6 post-infection.

(D) Gene Ontology analysis of genes that are downregulated with TPT treatment at days 4 (top) and 6 (bottom) post-infection.

(E) Representative hematoxylin and eosin (H&E) scan of lungs in DMSO-treated, infected hamsters at 4 days post-infection. Arrow indicates diffuse lung inflammatory damage, bronchiolar epithelium cell death, bronchiolar luminal secretion, and hemorrhage. Arrowheads indicate diffuse alveoli destruction with massive immune cell infiltration and exudation. Open arrows indicate vasculitis.

(F) Representative H&E scan of lungs in infected, DMSO-treated hamsters 6 days post-infection. Lung tissue consolidation affected most of the lung lobe examined. Arrowhead indicates bronchial secretion, infiltration and alveolar space exudation, immune cell infiltration, and hemorrhage. Arrow indicates alveolar and bronchiolar cell proliferation.

(G) Representative H&E scan of lungs in infected, TPT-treated hamsters 4 days post-infection showing diffuse milder inflammatory damage. Arrows indicate bronchiolar epithelium cell death with milder peribronchiolar infiltration. Arrowheads indicate diffuse alveolar wall thickening with capillary congestion. No conspicuous alveolar space infiltration, exudation, or hemorrhage was observed. Open arrows indicate that vasculitis is very mild and rare.

(H) Representative H&E scan of lungs in infected, TPT-treated hamsters 6 days post-infection showing patchy lung tissue consolidation with cell proliferation. Most alveolar areas are without exudation and infiltration.

Figure 2G) and increases in K27ac signals (positive delta H3K27ac levels; Figure 2H) and an increase in number of enhancers (Wilcoxon p = 0.015) compared to TOP1-independent genes. These differences are typical features of genes that are amenable for selective inhibition by transcriptional and epigenetic inhibitors (Marazzi et al., 2018).

To determine whether inhibition of TOP1 activity phenocopies depletion of TOP1 and dampens inflammatory gene expression, we treated SARS-CoV-2-infected A549-ACE2 cells with topotecan (TPT), a US Food and Drug Administration (FDA)-approved TOP1 inhibitor. TPT treatment, unlike DMSO treatment, dampens the expression of IL-6, CXCL2, CXCL3, CXCL8, EGR1, and TNFAIP3 (Figure S2A), similar to what we observed in siTOP1-treated cells (Figures 2B and 2D). Reduced inflammatory gene expression was not a result of a direct antiviral effect of TPT. Unlike remdesivir, a drug with known antiviral activity toward SARS-CoV-2, TPT does not inhibit viral replication (Figures S2B and S2C), suggesting that its activity is directed toward suppression of host gene expression.

TOP1 inhibition suppresses lung inflammation and lung damage in infected hamsters

To determine if inhibition of TOP1 activity can dampen inflammatory gene expression *in vivo*, we assessed the effects of TPT treatment in the golden Syrian hamster model (Muñoz-Fontela et al., 2020) (hereafter referred as hamster), a nonlethal model of SARS-CoV-2 infection (Imai et al., 2020; Sia et al., 2020).

We treated SARS-CoV-2-infected hamsters with either vehicle control (DMSO) or 10 mg/kg TPT at days 1 and 2 post-infection. Lungs from these animals were then collected for histology and transcriptome analysis at days 4 and 6 post-infection (Figure 3A).

Clustering of RNA-seq reads using principal-component analysis (PCA) indicates that the gene expression profiles under the three conditions (uninfected, infected/DMSO treated, and infected/TPT treated) partition based on infection, treatment status, and the temporality of the infection (days 4 and 6), with each replicate clustering in close proximity to its counterpart (Figure 3B).

Differential expression (DE) analysis showed that TPT suppresses inflammatory gene expression in the lungs of infected hamsters (Figures 3C and 3D; Tables S4A and S4B). Clustering of the DE data indicates that the gene expression profiles of TPT-treated infected lungs are more similar to that of the noninfected lungs rather than infected ones (Figure 3C). The GO categories associated with the TPT-suppressed genes indicates specific inhibition of virus-induced and inflammatory genes at

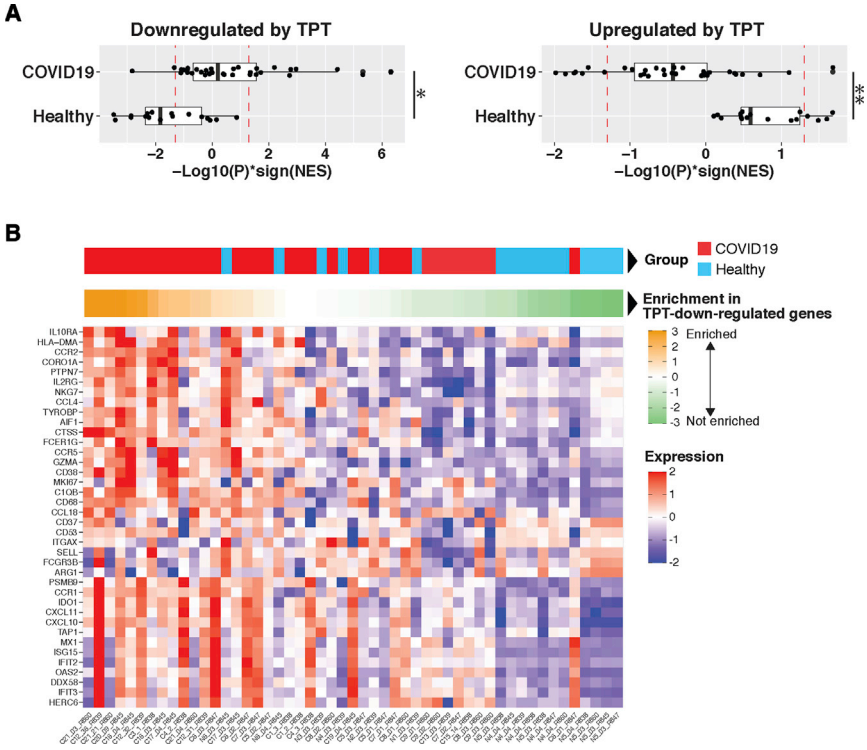

Figure 4. TPT suppresses gene programs upregulated in autopsy lung from COVID-19 patients

(A) GSEA of lung tissue gene expression profiles from COVID-19 deceased patients versus healthy patients (Nienhold et al., 2020). Signed −log10 adjusted p values indicate enrichment of down-regulated (top panel) and upregulated (bottom panel) gene signatures from TPT-treated hamsters infected with SARS-CoV-2. Sign of enrichment is given by the normalized enrichment score (NES). Dashed lines indicate a significance levels of p = 0.05. Differences in mean NES are shown. *p = 10^{-3}; **p = 5 × 10^{-4}, ***p = 10^{-7}.

(B) Expression in lung autopsy tissue of COVID-19 patients and healthy controls (Nienhold et al., 2020) of genes downregulated in TPT-treated SARS-CoV-2-infected hamsters (log2(absolute fold change [log2|FC|] > 1, false discovery rate [FDR] = 10%). Patient groups are indicated by the topmost bar. Gene set enrichment scores, calculated as −log10(p)*sign(NES), are indicated in the middle bar. The lower heatmap shows the individual gene expression profile of the indicated TPT-inhibited gene for a given patient (columns). Heatmap is sorted by column from the highest (left) to lowest enrichment score (right).

both day 4 and day 6 post-infection (Figure 3D; Tables S4C and S4D).

Histopathological analysis of infected, DMSO vehicle-treated hamster lungs at days 4 and 6 post-infection displayed diffused alveoli destruction, bronchiolar epithelium cell death, and hemorrhaging, coupled with massive immune cell infiltration and exudation, typically associated with increased expression of inflammatory mediators and recruitment of immune cells during infection (Figures 3E and 3F). On the contrary, TPT treatment diminished pathological features of lung damage in infected animals. Lungs from these animals did not have conspicuous alveolar space infiltration, exudation, or hemorrhaging at both days 4 and 6 post-infection (Figures 3G and 3H).

To determine the clinical significance of our observations, we then asked if the genes that were downregulated by TPT treatment in SARS-CoV-2-infected hamsters also corresponded to immunopathological gene signatures that have been observed in COVID-19 patients. Cross-comparison of our results with the gene expression profiles in human lungs isolated from autopsies of COVID-19 patients and uninfected control lungs (Nienhold et al., 2020) indicated that TPT-suppressed genes are hyperactivated in patients who succumbed to infection (Figures 4A and 4B). In fact, TPT-inhibited genes are genes that are upregulated in COVID-19 lung autopsy tissue relative to healthy control (p < 1E-3) (Figure 4A, left panel), while genes upregulated by TPT are downregulated in COVID-19 lung relative to control (p < 1E-7) (Figure 4A, right panel). These results suggest that treatment with TPT might reverse COVID-19-induced lung gene expression responses. The gene expression profiles of TPT-inhibited genes in individual patients (heatmap, Figure 4B) and the corresponding gene set enrichment scores are shown in Figure 4B.

SARS-CoV-2-infected epithelial cells induce limited type I and type II interferon responses (Blanco-Melo et al., 2020). Since we observe that these genes are downregulated in the presence of TPT in infected hamster lungs (Figure 3D), this suggested that TPT may also act on immune cells that are recruited to and/or activated in the lung upon infection. To determine if the TPT-dependent transcriptomic signature we observe is driven by suppression of inflammatory genes solely in epithelial cells or also from immune cells, we performed gene set enrichment analyses (GSEA) of gene expression profiles in immune cell types derived from single cell RNA seq (scRNA-seq) of the bronchoalveolar lavage fluid (BALF) from COVID-19 patients with severe disease or from healthy controls (Liao et al., 2020). Doing so allowed us to characterize immune-cell-type-specific transcriptome signatures during infection with SARS-CoV-2. Our analyses indicate that a subset of genes suppressed by TPT in our animal model are expressed specifically by immune cells (macrophage, neutrophil, and dendritic cells) isolated from severe COVID-19 cases and not in healthy controls (Figures S3A and S3B). Notably, an interferon-stimulated gene (ISG) signature appears to mainly reside in phagocytes; however, the nature of the cells that produce the interferons and the nature of the interferons themselves that drive ISGs remain largely unknown.

Immune cells are unlikely to be productively infected by SARS-CoV-2 (Banerjee et al., 2020a), so their infection-induced gene programs targeted by TPT treatment are most likely driven by PAMP/DAMP-dependent stimulation (e.g., viral RNA released from apoptotic cells) or cytokine signaling from bystander

infected epithelial cells. To determine if this is true, we performed *in vitro* experiments in THP-1, a human monocytic cell line. Our data indicate that TPT suppresses, in a concentration-dependent manner, inflammatory genes in response to purified SARS-CoV-2 viral RNA or supernatant from productively infected cells (Figure S3C). We were unable to detect productive SARS-CoV-2 infection of these cells, in line with a previous report (Banerjee et al., 2020a). Overall, our analyses support the idea that TPT is active in both epithelial and immune cells and suppresses inflammatory gene programs induced by the infection.

We next sought to validate whether lower dosages of TPT, which are associated with negligible cytostatic effects (Guichard et al., 2001; Houghton et al., 1995; Némati et al., 2010), were effective in suppressing SARS-CoV-2-infection-induced inflammation. We performed a parallel experiment to the one described in Figure 3A using 5-fold-lower dose of TPT (2 mg/kg) and the same regimen of TPT treatment at days 1 and 2 post-infection (Figure S4A). Lungs from infected and treated hamsters were assayed at day 4 post-infection.

Animals treated with TPT had reduced lung to body weight ratios post-infection (Figure S4B), which suggest reduced pulmonary edemas in these animals. In line with this, histopathological analyses showed reduced broncho-pneumonia (Figures S4C–S4E) and immune cell infiltration (Table S5) in the lungs of TPT-treated animals when compared to DMSO-treated ones. qPCR analysis of representative genes also suggested reduced expression of inflammatory genes in TPT-treated animals (Figure S4F).

Gene suppression and reduced lung damage occurred despite of a moderate 3-fold increase virus growth at day 4, where both TPT- and DMSO-treated lungs display similar viral titer. By day 8, virus growth in both TPT and DMSO treatment ceased to an undetectable level (Figure S4G), suggesting that TPT treatment does not change the overall kinetics of viral clearance.

Overall, these results suggest that lower doses of TPT treatment can still effectively suppress the expression of inflammatory molecules and ameliorate inflammation-induced pathology during SARS-CoV-2 infection. Our results therefore support the hypothesis that TPT suppresses SARS-CoV-2-induced lung inflammation *in vivo*.

TOP1 inhibition therapy suppresses SARS-CoV-2 morbidity and lethality in transgenic mice

To further verify our results, we extended our studies to a complementary model and evaluated the effects of TPT treatment in transgenic mice that express the human ACE2 receptor under the cytokeratin 18 gene promoter (K18-hACE2). This mouse strain is susceptible to SARS-CoV-2 infection and displays a disease progression profile that shares many features of severe COVID-19 (Winkler et al., 2020). Importantly, loss of pulmonary function and weight loss in these mice occurs after the peak of viral replication and coincides with infiltration of immune cells (monocytes, T cells, and neutrophils) in the lung and alveolar spaces at day 4 post-infection (Winkler et al., 2020). As such, K18-hACE2 has been suggested as a model to define the basis of SARS-CoV-2-induced lung disease and test immune and antiviral countermeasures (Bao et al., 2020; Winkler et al., 2020).

To test whether TPT-mediated reduction of inflammation provides a protective effect in infected K18-hACE2 mice, we performed three different regimes of TPT treatments, labeled as early, intermediate, and late, to respectively describe dosing of the inhibitor at 2 mg/kg on days 1+2, 3+4, or 4+5 post-infection respectively (Figures 5A and S5A).

The rationale behind this approach is that inhibition of inflammation could be detrimental during the early phases of the infection. The optimal protective effect of inhibiting inflammation should be achieved during the hyper-inflammatory phase of the disease, which would coincide with the later stage of infection. Late suppression of inflammatory response would have the added benefit of not altering early phases of the antiviral response. Indeed, our results showed that early and intermediate treatment of TPT is ineffective in reducing the morbidity and mortality caused by SARS-CoV-2 infection (Figures S5B and S5C), despite intermediate TPT treatment significantly delaying the onset of weight loss ($p = 0.0028$, two-way ANOVA [mixed effects]).

Strikingly, we found that late TPT treatment provided significant survival benefit ($p = 0.0085$, log-rank Mantel-Cox) to infected mice when compared to DMSO-vehicle-treated controls (Figure 5B). In addition, TPT significantly improved morbidity outcomes in infected mice. Despite an overall delay in weight loss kinetics in TPT mice (Figure 5C), fewer mice lost >15% of their body weight compared to DMSO-treated mice (Figure 5D; $p = 0.0409$, Fisher's exact test). Importantly, TPT administration did not significantly change viral titers immediately after treatment (day 7 post-infection, Figure 5E), nor did it delay viral clearance kinetics, as no detectable virus, as measured by plaque assays, was found in the lungs of both TPT- and DMSO-treated mice by day 14 post-infection (Figure 5E). As expected, TPT treatment was also associated with suppression of inflammatory gene expression in the lung, as indicated by qPCR of representative genes (Figure 5F) and supporting our initial hypotheses.

Finally, we assessed longer-term effects of TPT treatment in mice. TPT-treated mice survived past 9 weeks post-infection, with post-recovery weight gain levels (Figure 5G) similar to those of DMSO-treated mice. Levels of neutralizing antibody activity in the blood of DMSO- and TPT-treated mice were similar at 5 weeks post-infection (Figure 5H), suggesting that TPT treatment does not negatively impact adaptive immune responses.

Overall, our results indicate that inhibition of hyper-inflammation by therapeutic administration of TPT can rescue K18-hACE2 mice from lethal SARS-CoV-2 infection.

DISCUSSION

Although the pathophysiology of SARS-CoV-2 has not yet been fully characterized, it has been observed that SARS-CoV-2 infection triggers hyper-activation of pro-inflammatory cytokines (IL-6, IL-1β, and tumor necrosis factor α [TNF-α]) and chemokines (CXCL8, CXCL9, CXCL10, and CCL2) (Huang et al., 2020; Lucas et al., 2020; Merad and Martin, 2020; Tang et al., 2020; Zhou et al., 2020a). The increased level of inflammatory molecules has been shown to correlate with COVID-19 disease severity (Del Valle et al., 2020; Moore and June, 2020). While the exact mechanism and cell-type-specific contributions to hyper-inflammation still needs to be fully elucidated, monocytes,

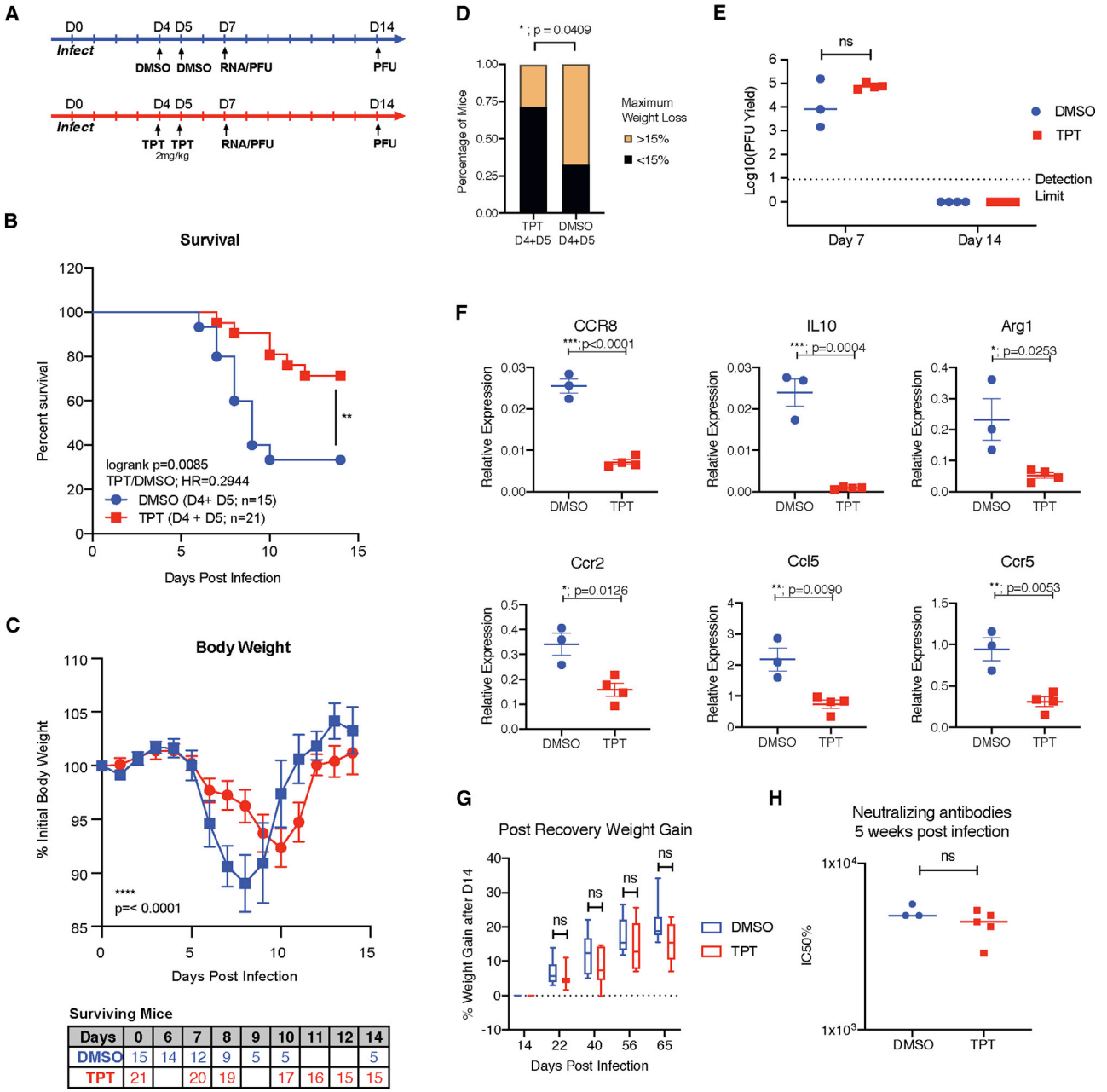

Figure 5. Late treatment of TPT in K18-hACE2 mice provides survival benefit during SARS-CoV-2 infection

(A) Schematic describing treatment regime used in mice.

(B) Survival curve of K18-hACE2 mice infected with 1E4 plaque-forming units (PFUs) SARS-CoV-2. Mice were treated with either DMSO vehicle control (n = 15; DMSO, blue) or 2 mg/kg TPT (n = 21; TPT, red) at days 4 and 5 post-infection. p values were determined by log-rank (Mantel-Cox) test, and hazard ratios (log-rank) are shown. **p < 0.01.

(C) Corresponding curves showing the average body weight of mice relative to their initial starting weights through the course of the infection with 1E4 PFU SARS-CoV-2. The number of mice at each day is indicated in the table below. **p < 0.01, by two way mixed model ANOVA. Error bars show the mean and SEM of mice (DMSO, n = 15; TPT n = 21).

(D) Percentage of DMSO- or TPT-treated mice that have a maximum weight loss of ≤15% or >15% of their starting weights. *p < 0.05, Fisher's exact test.

(E) Viral titers in the lungs of DMSO- or TPT-treated SARS-CoV-2-infected mice at days 7 and 14 post-infection. ns, not significant by two-tailed Student's t test. Mean and SEM are shown.

(legend continued on next page)

macrophages, and dendritic cells are primary candidates and have been reported to contribute to the cytokine-mediated immunopathology seen in human (Del Valle et al., 2020; Giamarellos-Bourboulis et al., 2020; Moore and June, 2020). This is supported by previous studies of the immune response against SARS-CoV-1 and Middle East Respiratory Syndrome Coronavirus (MERS-CoV) infections (Cheung et al., 2005; Wong et al., 2004). Additionally, non-myeloid cells have been recently shown to contribute to the hyper-inflammatory program (Zhou et al., 2020b). Elevated inflammatory responses contribute to sepsis and multi-organ failure, major causes of death from COVID-19 (Zhou et al., 2020a). Therefore, treatments that can suppress host inflammatory response might be effective therapeutic strategies for COVID-19. In this light, it is important to highlight that glucocorticoids (dexamethasone, methylprednisolone, and hydrocortisone), which act as suppressors of systemic inflammation, have been reported to ameliorate the outcome of COVID-19, especially in hospitalized patients who require supplemental oxygen (WHO REACT Working Group et al., 2020).

Chromatin structure and function upon infection

While our knowledge of SARS-CoV-2 pathogenesis is expanding rapidly, little is known about how epigenetic modifications and genome structure are affected by infection and in what capacity they affect gene activity (Liu et al., 2020). Our data suggest that SARS-CoV-2 infection imposes both global and local (gene-specific) effects on host chromatin, ultimately dictating gene induction and suppression, and the establishment of a gene expression program in the infected cell.

Regarding SARS-CoV-2-infection-induced compartment movement, we surmise that A-B (active to inactive) and B-A (inactive to active) switches are driven by transcriptional and epigenome activity. While A-B transitions are characterized by decreased K27ac at promoters and gene suppression, B-A is accompanied by increased K27ac at promoters and enhancers, enhancer-promoter interactions, and transcriptional induction. Gene suppression has functional consequences, as it affects many conventional infection-induced genes activated by STAT1/2 and IRF3 transcription factors. Suppression is likely a result of viral antagonism. Gene activation is the result of signal-induced transactivation and indicates that many cellular genes escape viral suppression during infection. One prominent example is a subset of inflammatory genes whose expression is driven by infection-activated transcription factor NF-κB. The proteins encoded by these genes are potent pro-inflammatory molecules and present systemically with high levels in severe COVID-19 patients (Del Valle et al., 2020; Moore and June, 2020). The selective and concerted induction of inflammatory genes provides the rationale for using epigenetic inhibitors to suppress their induction and establish a global anti-inflammatory state (Marazzi et al., 2018).

Inflammatory gene suppression therapy

We show that the host enzyme TOP1 promotes transcriptional activation of pro-inflammatory genes during SARS-CoV-2 infection. We then demonstrate that TOP1 inhibition limits the expression of inflammatory genes in the lungs of infected animals. Most importantly, TOP1 inhibition decreases morbidity and morbidity in infected mice. The therapeutic effect can be achieved by drug administration 4–5 days following infection.

The suppression of inflammation *in vivo* is most likely the result of not only a dampened epithelial response but also neutrophil/monocytic cell activation and response. Based on our experiments and gene signature analyses of specific cell types, we posit that TPT suppresses inducible transcriptional programs in both infected and bystander cells. Dampening highly inducible genes and sparing housekeeper genes is a typical feature of epigenetic inhibitors that act on signal-induced genes, which aside from the requirement of cofactors for their activation have unifying genomic features like high burst rates conferred by many regulatory enhancers (Chen et al., 2019; Fukaya et al., 2016; Marazzi et al., 2018; Senecal et al., 2014; Zabidi et al., 2015).

Lethal inflammation in severe COVID-19 has been associated with the dysregulation of multiple inflammatory genes, including IL-6, IL-1, and IL-10. However, many of the current strategies proposed to treat severe COVID-19, such as anti-IL-6 (e.g., tocilizumab and sarilumab) or anti-IL-1 (e.g., anakinra) inhibitors, are directed against single inflammatory mediators and specific gene expression programs. The effects of such drugs may be undermined by alternative gene activation pathways driven by other cytokines/transcription factors.

In contrast, TPT functions to broadly dampen inflammatory gene expression programs, regardless of the cell or activation pathways. Inhibition of systemic inflammation using the glucocorticoid dexamethasone has been shown to provide survival benefit to severe COVID-19 patients, suggesting that this is indeed a viable strategy. That being said, it is important to note that TPT and glucocorticoids have different molecular targets and exert anti-inflammatory effects via different molecular mechanisms of action.

Finally, TPT and other TOP1 inhibitors like irinotecan are widely available and FDA approved. Irinotecan is in the World Health Organization (WHO) list of essential medicines. They are inexpensive, and generic formulation exists throughout the world, making them easily accessible for immediate use. Overall, our results suggest that repurposing of TOP1 inhibitor could be a valuable strategy to treat severe COVID-19.

Limitations of study

Our study indicates a promising effect of TPT in COVID-19 in preclinical animal models. As with any animal model, they are only partially representative of the biology of humans. In our animal models, we can suppress inflammation and reduce disease pathology in the lung using two doses of TOP1 inhibition therapy

(F) qPCR analysis of the indicated inflammatory genes at days 7 post-infection. ns, not significant; *p < 0.05; **p < 0.01; ***p < 0.001; ****p < 0.0001 by two-tailed Students t test. Each point represents an individual mouse. Means and SD are shown. Data are normalized to hypoxanthine guanine phosphoribosyl transferase (HPRT) expression in each sample.

(G) Post-recovery weight gain at the indicated days post-infection in DMSO-treated (n = 8) or TPT-day 4+5-treated (n = 8) mice. Weights are normalized to the weights of mice at day 14 post-infection. ns, not significant, by Students' t test.

(H) Neutralizing antibody titers in DMSO or TPT-treated mice. ns, not significant by two-tailed Students' t test. Mean and SEM are shown.

with TPT at 2 mg/kg intraperitoneally. This equates to a 5-fold reduction from typical chemotherapeutic anti-cancer doses in rodent models (Guichard et al., 2001; Houghton et al., 1995; Némati et al., 2010). In clinical practice, the TOP1 inhibitors TPT and irinotecan have well-characterized pharmacokinetics and toxicity profiles (Kollmannsberger et al., 1999; Mathijssen et al., 2001), albeit in patients without SARS-CoV-2 infection.

Doses that are 5-fold lower than those used in the treatment of small-cell lung cancer (TPT) (Rowinsky et al., 1992; von Pawel et al., 1999) and colorectal cancer (irinotecan) (André et al., 1999) are expected to cause little to no toxicity and, importantly, no risk of neutropenia. Nonetheless, safety trials of the reduced dosage of TPT or irinotecan in COVID-19 patients will need to be performed prior to testing efficacy.

Another important consideration is that the window of opportunity for TOP1 inhibitor treatment in humans needs to be carefully evaluated. Many reports indicate that the timing of the intervention against coronaviruses is key, as protective antiviral and damaging excessive inflammatory responses need to be balanced (Channappanavar et al., 2016, 2019; Grajales-Reyes and Colonna, 2020). Our data align with those studies, as early treatment of TPT did not display protective effect in mice.

In essence, stratification of patients based on inflammatory marker is key, as suppressing gene programs too early during infection might compromise antiviral response together with limiting inflammatory responses, with the unwanted effect of increasing viral replication and dissemination. Accordingly, glucocorticoids can lead to increase in viral persistence in convalescent severe patients. Similarly, corticosteroid treatment has been suggested to have negative effects post-recovery in patients with non-severe COVID-19.

In line with this, inhibition of inflammation by TPT or other molecules that lower systemic inflammation could theoretically lead to a resurgence in viral replication and administration of an antiviral agent with activity against SARS-CoV-2 after anti-inflammatory therapy should be used.

The safety and efficacy of our strategy will now be evaluated in two clinical trials of TPT that have been submitted for trial initiation. Lastly, we strongly discourage any "off label" use of TOP1 inhibitors until safety and effectiveness is established by clinical trials.

STAR★METHODS

Detailed methods are provided in the online version of this paper and include the following:

- KEY RESOURCES TABLE
- RESOURCE AVAILABILITY
  - Lead contact
  - Materials availability
  - Data and code availability
- EXPERIMENTAL MODEL AND SUBJECT DETAILS
  - Cells
  - Viral strains
- METHOD DETAILS
  - Generation of A549-ACE2 cells
  - Preparation of siTOP1 sequencing libraries
  - ChIP-seq library preparation
  - Preparation of HiC libraries
  - Preparation of hamster RNA sequencing libraries
  - Hamster infections
  - K18-hACE2 mice infections
  - Extraction of RNA from lungs of infected hamsters and mice
  - Histological analysis
  - Promoter capture Hi-C (PCHi-C)
  - Quantification of viral titers by plaque assays
  - Quantification of neutralizing antibodies in serum (microneutralization assays)
  - TPT treatment of SARS-CoV-2 infected A549-ACE2 cells
  - TPT treatment of THP1 cells
  - Viral growth and cytotoxicity assays in the presence of TPT or Remdesivir
- QUANTIFICATION AND STATISTICAL ANALYSIS
  - Mouse infection studies
  - Quantitative qPCR assays
  - Illumina short read RNA sequencing analyses
  - GSEA analysis for gene signatures in TPT treated hamsters
  - ChIP-seq analysis
  - HiC analysis
  - Promoter capture Hi-C analysis

SUPPLEMENTAL INFORMATION

Supplemental information can be found online at https://doi.org/10.1016/j.cell.2021.03.051.

ACKNOWLEDGMENTS

We thank the staff of KSU Biosecurity Research Institute; the histological laboratory at the Kansas State Veterinary Diagnostic Laboratory (KSVDL); members of the Histology and Immunohistochemistry sections at the Louisiana Animal Disease Diagnostic Laboratory (LADDL); the CMG staff; and Bianca Artiaga, Dashzeveg Bold, Konner Cool, Emily Gilbert-Esparza, Chester McDowell, and Yonghai Li. We thank the teams at the Icahn School of Medicine at Mount Sinai, the Genomics and Mouse facilities, and Alan Soto from the Biorepository and Pathology Dean's CoRE. We thank Cindy Beharry, Nanyi Julia Zhao, Nancy Francoeur, Nataly Fishman, Marion Dejosez, Thomas Zwaka, and Carles Martinez-Romero for their help and advice. Luis Martinez (Texas Biomedical Research Institute) and the Center for Therapeutic Antibody Development (CTAD) (Thomas Moran, Andy Duty, and Thomas Kraus) kindly provided the NP1C7C7 antibody.This work was partially supported through grants from NBAF Transition Funds and the NIAID Centers of Excellence for Influenza Research and Surveillance (CEIRS) under contract number HHSN 272201400006C to A.G.-S.; the Department of Homeland Security Center of Excellence for Emerging and Zoonotic Animal Diseases under grant HSHQDC-16-A-B0006 to J.A.R.; CRIP (Center for Research for Influenza Pathogenesis CEIRS, contract HHSN272201400008C); supplements to NIAID grant U19AI135972 and DOD grant W81XWH-20-1-0270; the Defense Advanced Research Projects Agency (HR0011-19-2-0020); and the JPB Foundation, the Open Philanthropy Project (research grant 2020-215611 [5384]), and anonymous donors. S.Y. received funding from a Swiss National Foundation (SNF) Early Postdoc.Mobility fellowship (P2GEP3_184202). This work was partially supported by funding to I. Marazzi., specifically the Burroughs Wellcome Fund (United States; 1017892), the Chan Zuckerberg Initiative (United States; 2018-191895), the Hirschl Young Investigator fellowship, and NIH grants U01AI150748 and R01AI143840. Partial support by the AMP Core of

the Center of Emerging and Zoonotic Infectious Diseases of the National Institutes of Health under award number P20GM130448 to J.R.

AUTHOR CONTRIBUTIONS

Conceptualization, I. Marazzi; investigation: J.S.Y.H., B.W.-Y.M., L.C., T.J., S.Y., S.P., J.A.W., N.N.G., D.A.M., S.V.I., I. Morozov, J.D.T., Y.S.F., R.R., Z.Z., S.Z., N.Z., B.S.M., H.R.-J., V.M., M.J.T., S.-Y.L., S.J., A.E., H.L., A.J.Z., A.C.-Y.L., W.-C.L., T.A., A.M., R.A.A., M. Schotsaert, and S.H.; genomics analyses (epigenetics): S.P., J.A.W., E.R.M., and M.T.W.; genomics analyses (chromatin structure), S.H. and C.B.; GSEA, J.A.W. and E.R.M.; data analyses (others), J.S.Y.H., Y.S.F., H.R.-J., V.M., and M. Spivakov; *in vivo* study and veterinarian analysis, J.S.Y.H., B.W.Y.M., L.C., S.Y., H.L., A.J.Z., A.C.-Y.L., H.C., N.N.G., D.A.M., S.V.I., I. Morozov, J.D.T., J.A.R., M.C., and U.B.R.B.; histology and medical consultation, E.S., D.K., A.M., J.B., and A.D.J.; writing – original draft, I. Marazzi; resources, K.W., M.J.T., R.S., A.G.-S., B.R.T., and S.K.C.; writing – review & editing, J.S.Y.H., Z.Z., E.G., E.S., D.A.K., M.B., E.R.M., A.G.-S., M.T.W., S.H., C.B., J.A.R., and I. Marazzi; funding acquisition, A.G.-S., H.C., C.B., J.A.R., I. Marazzi; project administration, I. Marazzi; supervision, I. Marazzi.

DECLARATION OF INTERESTS

The García-Sastre Laboratory has received research support from Pfizer, Senhwa Biosciences, 7 Hills Pharma, Pharmamar, Blade Therapuetics, Avimex, Johnson & Johnson, Dynavax, Kenall Manufacturing, and ImmunityBio. A.G.-S. has consulting agreements for the following companies involving cash and/or stock: Vivaldi Biosciences, Contrafect, 7 Hills Pharma, Avimex, Vaxalto, Accurius, and Esperovax. M.J.T. is an employee of Enhanc3D Genomics. M. Spivakov is a co-founder of Enhanc3D Genomics. I. Marazzi is an inventor in the patent WO2017106466A1

Received: December 1, 2020
Revised: February 5, 2021
Accepted: March 24, 2021
Published: March 30, 2021

REFERENCES

Amanat, F., Stadlbauer, D., Strohmeier, S., Nguyen, T.H.O., Chromikova, V., McMahon, M., Jiang, K., Arunkumar, G.A., Jurczyszak, D., Polanco, J., et al. (2020). A serological assay to detect SARS-CoV-2 seroconversion in humans. Nat. Med. *26*, 1033–1036.

Amemiya, H.M., Kundaje, A., and Boyle, A.P. (2019). The ENCODE Blacklist: Identification of Problematic Regions of the Genome. Sci. Rep. *9*, 9354.

André, T., Louvet, C., Maindrault-Goebel, F., Couteau, C., Mabro, M., Lotz, J.P., Gilles-Amar, V., Krulik, M., Carola, E., Izrael, V., and de Gramont, A. (1999). CPT-11 (irinotecan) addition to bimonthly, high-dose leucovorin and bolus and continuous-infusion 5-fluorouracil (FOLFIRI) for pretreated metastatic colorectal cancer. GERCOR. Eur. J. Cancer *35*, 1343–1347.

Banerjee, A., Nasir, J.A., Budylowski, P., Yip, L., Aftanas, P., Christie, N., Ghalami, A., Baid, K., Raphenya, A.R., Hirota, J.A., et al. (2020a). Isolation, Sequence, Infectivity, and Replication Kinetics of Severe Acute Respiratory Syndrome Coronavirus 2. Emerg. Infect. Dis. *26*, 2054–2063.

Banerjee, A.K., Blanco, M.R., Bruce, E.A., Honson, D.D., Chen, L.M., Chow, A., Bhat, P., Ollikainen, N., Quinodoz, S.A., Loney, C., et al. (2020b). SARS-CoV-2 Disrupts Splicing, Translation, and Protein Trafficking to Suppress Host Defenses. Cell *183*, 1325–1339.e21.

Bao, L., Deng, W., Huang, B., Gao, H., Liu, J., Ren, L., Wei, Q., Yu, P., Xu, Y., Qi, F., et al. (2020). The pathogenicity of SARS-CoV-2 in hACE2 transgenic mice. Nature *583*, 830–833.

Blanco-Melo, D., Nilsson-Payant, B.E., Liu, W.C., Uhl, S., Hoagland, D., Møller, R., Jordan, T.X., Oishi, K., Panis, M., Sachs, D., et al. (2020). Imbalanced Host Response to SARS-CoV-2 Drives Development of COVID-19. Cell *181*, 1036–1045.e9.

Bost, P., Giladi, A., Liu, Y., Bendjelal, Y., Xu, G., David, E., Blecher-Gonen, R., Cohen, M., Medaglia, C., Li, H., et al. (2020). Host-Viral Infection Maps Reveal Signatures of Severe COVID-19 Patients. Cell *181*, 1475–1488.e12.

Cairns, J., Freire-Pritchett, P., Wingett, S.W., Várnai, C., Dimond, A., Plagnol, V., Zerbino, D., Schoenfelder, S., Javierre, B.M., Osborne, C., et al. (2016). CHiCAGO: robust detection of DNA looping interactions in Capture Hi-C data. Genome Biol. *17*, 127.

Channappanavar, R., and Perlman, S. (2017). Pathogenic human coronavirus infections: causes and consequences of cytokine storm and immunopathology. Semin. Immunopathol. *39*, 529–539.

Channappanavar, R., Fehr, A.R., Vijay, R., Mack, M., Zhao, J., Meyerholz, D.K., and Perlman, S. (2016). Dysregulated Type I Interferon and Inflammatory Monocyte-Macrophage Responses Cause Lethal Pneumonia in SARS-CoV-Infected Mice. Cell Host Microbe *19*, 181–193.

Channappanavar, R., Fehr, A.R., Zheng, J., Wohlford-Lenane, C., Abrahante, J.E., Mack, M., Sompallae, R., McCray, P.B., Jr., Meyerholz, D.K., and Perlman, S. (2019). IFN-I response timing relative to virus replication determines MERS coronavirus infection outcomes. J. Clin. Invest. *129*, 3625–3639.

Chen, L.F., Lin, Y.T., Gallegos, D.A., Hazlett, M.F., Gómez-Schiavon, M., Yang, M.G., Kalmeta, B., Zhou, A.S., Holtzman, L., Gersbach, C.A., et al. (2019). Enhancer Histone Acetylation Modulates Transcriptional Bursting Dynamics of Neuronal Activity-Inducible Genes. Cell Rep. *26*, 1174–1188.e5.

Cheung, C.Y., Poon, L.L., Ng, I.H., Luk, W., Sia, S.F., Wu, M.H., Chan, K.H., Yuen, K.Y., Gordon, S., Guan, Y., and Peiris, J.S. (2005). Cytokine responses in severe acute respiratory syndrome coronavirus-infected macrophages in vitro: possible relevance to pathogenesis. J. Virol. *79*, 7819–7826.

Daniloski, Z., Jordan, T.X., Wessels, H.H., Hoagland, D.A., Kasela, S., Legut, M., Maniatis, S., Mimitou, E.P., Lu, L., Geller, E., et al. (2021). Identification of Required Host Factors for SARS-CoV-2 Infection in Human Cells. Cell *184*, 92–105.e16.

Del Valle, D.M., Kim-Schulze, S., Huang, H.H., Beckmann, N.D., Nirenberg, S., Wang, B., Lavin, Y., Swartz, T.H., Madduri, D., Stock, A., et al. (2020). An inflammatory cytokine signature predicts COVID-19 severity and survival. Nat. Med. *26*, 1636–1643.

Dobin, A., Davis, C.A., Schlesinger, F., Drenkow, J., Zaleski, C., Jha, S., Batut, P., Chaisson, M., and Gingeras, T.R. (2013). STAR: ultrafast universal RNA-seq aligner. Bioinformatics *29*, 15–21.

Fukaya, T., Lim, B., and Levine, M. (2016). Enhancer Control of Transcriptional Bursting. Cell *166*, 358–368.

Giamarellos-Bourboulis, E.J., Netea, M.G., Rovina, N., Akinosoglou, K., Antoniadou, A., Antonakos, N., Damoraki, G., Gkavogianni, T., Adami, M.E., Katsaounou, P., et al. (2020). Complex Immune Dysregulation in COVID-19 Patients with Severe Respiratory Failure. Cell Host Microbe *27*, 992–1000.e3.

Gordon, D.E., Jang, G.M., Bouhaddou, M., Xu, J., Obernier, K., White, K.M., O'Meara, M.J., Rezelj, V.V., Guo, J.Z., Swaney, D.L., et al. (2020). A SARS-CoV-2 protein interaction map reveals targets for drug repurposing. Nature *583*, 459–468.

Grajales-Reyes, G.E., and Colonna, M. (2020). Interferon responses in viral pneumonias. Science *369*, 626–627.

Guichard, S., Montazeri, A., Chatelut, E., Hennebelle, I., Bugat, R., and Canal, P. (2001). Schedule-dependent activity of topotecan in OVCAR-3 ovarian carcinoma xenograft: pharmacokinetic and pharmacodynamic evaluation. Clin. Cancer Res. *7*, 3222–3228.

Heinz, S., Benner, C., Spann, N., Bertolino, E., Lin, Y.C., Laslo, P., Cheng, J.X., Murre, C., Singh, H., and Glass, C.K. (2010). Simple combinations of lineage-determining transcription factors prime cis-regulatory elements required for macrophage and B cell identities. Mol. Cell *38*, 576–589.

Heinz, S., Texari, L., Hayes, M.G.B., Urbanowski, M., Chang, M.W., Givarkes, N., Rialdi, A., White, K.M., Albrecht, R.A., Pache, L., et al. (2018). Transcription Elongation Can Affect Genome 3D Structure. Cell *174*, 1522–1536.e1522.

Hermine, O., Mariette, X., Tharaux, P.L., Resche-Rigon, M., Porcher, R., and Ravaud, P.; CORIMUNO-19 Collaborative Group (2021). Effect of Tocilizumab

vs Usual Care in Adults Hospitalized With COVID-19 and Moderate or Severe Pneumonia: A Randomized Clinical Trial. JAMA Intern. Med. *181*, 32–40.

Houghton, P.J., Cheshire, P.J., Hallman, J.D., 2nd, Lutz, L., Friedman, H.S., Danks, M.K., and Houghton, J.A. (1995). Efficacy of topoisomerase I inhibitors, topotecan and irinotecan, administered at low dose levels in protracted schedules to mice bearing xenografts of human tumors. Cancer Chemother. Pharmacol. *36*, 393–403.

Huang, C., Wang, Y., Li, X., Ren, L., Zhao, J., Hu, Y., Zhang, L., Fan, G., Xu, J., Gu, X., et al. (2020). Clinical features of patients infected with 2019 novel coronavirus in Wuhan, China. Lancet *395*, 497–506.

Imai, M., Iwatsuki-Horimoto, K., Hatta, M., Loeber, S., Halfmann, P.J., Nakajima, N., Watanabe, T., Ujie, M., Takahashi, K., Ito, M., et al. (2020). Syrian hamsters as a small animal model for SARS-CoV-2 infection and countermeasure development. Proc. Natl. Acad. Sci. USA *117*, 16587–16595.

Kollmannsberger, C., Mross, K., Jakob, A., Kanz, L., and Bokemeyer, C. (1999). Topotecan - A novel topoisomerase I inhibitor: pharmacology and clinical experience. Oncology *56*, 1–12.

Korotkevich, G., Sukhov, V., and Sergushichev, A. (2019). Fast gene set enrichment analysis. bioRxiv, 060012.

Lambert, S.A., Yang, A.W.H., Sasse, A., Cowley, G., Albu, M., Caddick, M.X., Morris, Q.D., Weirauch, M.T., and Hughes, T.R. (2019). Similarity regression predicts evolution of transcription factor sequence specificity. Nat. Genet. *51*, 981–989.

Langmead, B., and Salzberg, S.L. (2012). Fast gapped-read alignment with Bowtie 2. Nat. Methods *9*, 357–359.

Law, C.W., Chen, Y., Shi, W., and Smyth, G.K. (2014). voom: Precision weights unlock linear model analysis tools for RNA-seq read counts. Genome Biol. *15*, R29.

Lee, S., Channappanavar, R., and Kanneganti, T.D. (2020). Coronaviruses: Innate Immunity, Inflammasome Activation, Inflammatory Cell Death, and Cytokines. Trends Immunol. *41*, 1083–1099.

Lei, X., Dong, X., Ma, R., Wang, W., Xiao, X., Tian, Z., Wang, C., Wang, Y., Li, L., Ren, L., et al. (2020). Activation and evasion of type I interferon responses by SARS-CoV-2. Nat. Commun. *11*, 3810.

Li, H., Handsaker, B., Wysoker, A., Fennell, T., Ruan, J., Homer, N., Marth, G., Abecasis, G., and Durbin, R.; 1000 Genome Project Data Processing Subgroup (2009). The Sequence Alignment/Map format and SAMtools. Bioinformatics *25*, 2078–2079.

Liao, Y., Smyth, G.K., and Shi, W. (2014). featureCounts: an efficient general purpose program for assigning sequence reads to genomic features. Bioinformatics *30*, 923–930.

Liao, M., Liu, Y., Yuan, J., Wen, Y., Xu, G., Zhao, J., Cheng, L., Li, J., Wang, X., Wang, F., et al. (2020). Single-cell landscape of bronchoalveolar immune cells in patients with COVID-19. Nat. Med. *26*, 842–844.

Lin, Y.C., Benner, C., Mansson, R., Heinz, S., Miyazaki, K., Miyazaki, M., Chandra, V., Bossen, C., Glass, C.K., and Murre, C. (2012). Global changes in the nuclear positioning of genes and intra- and interdomain genomic interactions that orchestrate B cell fate. Nat. Immunol. *13*, 1196–1204.

Liu, X., Hong, T., Parameswaran, S., Ernst, K., Marazzi, I., Weirauch, M.T., and Fuxman Bass, J.I. (2020). Human Virus Transcriptional Regulators. Cell *182*, 24–37.

Love, M.I., Huber, W., and Anders, S. (2014). Moderated estimation of fold change and dispersion for RNA-seq data with DESeq2. Genome Biol. *15*, 550.

Lucas, C., Wong, P., Klein, J., Castro, T.B.R., Silva, J., Sundaram, M., Ellingson, M.K., Mao, T., Oh, J.E., Israelow, B., et al.; Yale IMPACT Team (2020). Longitudinal analyses reveal immunological misfiring in severe COVID-19. Nature *584*, 463–469.

Marazzi, I., Ho, J.S., Kim, J., Manicassamy, B., Dewell, S., Albrecht, R.A., Seibert, C.W., Schaefer, U., Jeffrey, K.L., Prinjha, R.K., et al. (2012). Suppression of the antiviral response by an influenza histone mimic. Nature *483*, 428–433.

Marazzi, I., Greenbaum, B.D., Low, D.H.P., and Guccione, E. (2018). Chromatin dependencies in cancer and inflammation. Nat. Rev. Mol. Cell Biol. *19*, 245–261.

Martin, M. (2011). Cutadapt removes adapter sequences from high-throughput sequencing reads. EMBnet.journal *17*, 3.

Mathijssen, R.H., van Alphen, R.J., Verweij, J., Loos, W.J., Nooter, K., Stoter, G., and Sparreboom, A. (2001). Clinical pharmacokinetics and metabolism of irinotecan (CPT-11). Clin. Cancer Res. *7*, 2182–2194.

McGinnis, C.S., Murrow, L.M., and Gartner, Z.J. (2019). DoubletFinder: Doublet Detection in Single-Cell RNA Sequencing Data Using Artificial Nearest Neighbors. Cell Syst. *8*, 329–337.e4.

Merad, M., and Martin, J.C. (2020). Pathological inflammation in patients with COVID-19: a key role for monocytes and macrophages. Nat. Rev. Immunol. *20*, 355–362.

Miller, M.S., Rialdi, A., Ho, J.S., Tilove, M., Martinez-Gil, L., Moshkina, N.P., Peralta, Z., Noel, J., Melegari, C., Maestre, A.M., et al. (2015). Senataxin suppresses the antiviral transcriptional response and controls viral biogenesis. Nat. Immunol. *16*, 485–494.

Moore, J.B., and June, C.H. (2020). Cytokine release syndrome in severe COVID-19. Science *368*, 473–474.

Muñoz-Fontela, C., Dowling, W.E., Funnell, S.G.P., Gsell, P.S., Riveros-Balta, A.X., Albrecht, R.A., Andersen, H., Baric, R.S., Carroll, M.W., Cavaleri, M., et al. (2020). Animal models for COVID-19. Nature *586*, 509–515.

Nagano, T., Lubling, Y., Várnai, C., Dudley, C., Leung, W., Baran, Y., Mendelson Cohen, N., Wingett, S., Fraser, P., and Tanay, A. (2017). Cell-cycle dynamics of chromosomal organization at single-cell resolution. Nature *547*, 61–67.

Némati, F., Daniel, C., Arvelo, F., Legrier, M.E., Froget, B., Livartowski, A., Assayag, F., Bourgeois, Y., Poupon, M.F., and Decaudin, D. (2010). Clinical relevance of human cancer xenografts as a tool for preclinical assessment: example of in-vivo evaluation of topotecan-based chemotherapy in a panel of human small-cell lung cancer xenografts. Anticancer Drugs *21*, 25–32.

Nicodeme, E., Jeffrey, K.L., Schaefer, U., Beinke, S., Dewell, S., Chung, C.W., Chandwani, R., Marazzi, I., Wilson, P., Coste, H., et al. (2010). Suppression of inflammation by a synthetic histone mimic. Nature *468*, 1119–1123.

Nienhold, R., Ciani, Y., Koelzer, V.H., Tzankov, A., Haslbauer, J.D., Menter, T., Schwab, N., Henkel, M., Frank, A., Zsikla, V., et al. (2020). Two distinct immunopathological profiles in autopsy lungs of COVID-19. Nat. Commun. *11*, 5086.

Pedregosa, F., Varoquaux, G., Gramfort, A., Michel, V., Thirion, B., Grisel, O., Blondel, M., Prettenhofer, P., Weiss, R., Dubourg, V., et al. (2011). Scikit-learn: Machine Learning in Python. J. Mach. Learn. Res. *12*, 2825–2830.

Quinlan, A.R., and Hall, I.M. (2010). BEDTools: a flexible suite of utilities for comparing genomic features. Bioinformatics *26*, 841–842.

Rao, S.S.P., Huang, S.C., Glenn St Hilaire, B., Engreitz, J.M., Perez, E.M., Kieffer-Kwon, K.R., Sanborn, A.L., Johnstone, S.E., Bascom, G.D., Bochkov, I.D., et al. (2017). Cohesin Loss Eliminates All Loop Domains. Cell *171*, 305–320.e24.

Rialdi, A., Campisi, L., Zhao, N., Lagda, A.C., Pietzsch, C., Ho, J.S.Y., Martinez-Gil, L., Fenouil, R., Chen, X., Edwards, M., et al. (2016). Topoisomerase 1 inhibition suppresses inflammatory genes and protects from death by inflammation. Science *352*, aad7993.

Ritchie, M.E., Phipson, B., Wu, D., Hu, Y., Law, C.W., Shi, W., and Smyth, G.K. (2015). limma powers differential expression analyses for RNA-sequencing and microarray studies. Nucleic Acids Res. *43*, e47.

Rowinsky, E.K., Grochow, L.B., Hendricks, C.B., Ettinger, D.S., Forastiere, A.A., Hurowitz, L.A., McGuire, W.P., Sartorius, S.E., Lubejko, B.G., Kaufmann, S.H., et al. (1992). Phase I and pharmacologic study of topotecan: a novel topoisomerase I inhibitor. J. Clin. Oncol. *10*, 647–656.

Salvarani, C., Dolci, G., Massari, M., Merlo, D.F., Cavuto, S., Savoldi, L., Bruzzi, P., Boni, F., Braglia, L., Turra, C., et al. (2021). Effect of Tocilizumab vs Standard Care on Clinical Worsening in Patients Hospitalized With COVID-19 Pneumonia: A Randomized Clinical Trial. JAMA Intern. Med. *181*, 24–31.

Schoenfelder, S., Furlan-Magaril, M., Mifsud, B., Tavares-Cadete, F., Sugar, R., Javierre, B.M., Nagano, T., Katsman, Y., Sakthidevi, M., Wingett, S.W.,

et al. (2015). The pluripotent regulatory circuitry connecting promoters to their long-range interacting elements. Genome Res. *25*, 582–597.

Schwarzer, W., Abdennur, N., Goloborodko, A., Pekowska, A., Fudenberg, G., Loe-Mie, Y., Fonseca, N.A., Huber, W., Haering, C.H., Mirny, L., and Spitz, F. (2017). Two independent modes of chromatin organization revealed by cohesin removal. Nature *551*, 51–56.

Senecal, A., Munsky, B., Proux, F., Ly, N., Braye, F.E., Zimmer, C., Mueller, F., and Darzacq, X. (2014). Transcription factors modulate c-Fos transcriptional bursts. Cell Rep. *8*, 75–83.

Sia, S.F., Yan, L.M., Chin, A.W.H., Fung, K., Choy, K.T., Wong, A.Y.L., Kaewpreedee, P., Perera, R.A.P.M., Poon, L.L.M., Nicholls, J.M., et al. (2020). Pathogenesis and transmission of SARS-CoV-2 in golden hamsters. Nature *583*, 834–838.

Siddiqi, H.K., and Mehra, M.R. (2020). COVID-19 illness in native and immunosuppressed states: A clinical-therapeutic staging proposal. J. Heart Lung Transplant. *39*, 405–407.

Stuart, T., Butler, A., Hoffman, P., Hafemeister, C., Papalexi, E., Mauck, W.M., 3rd, Hao, Y., Stoeckius, M., Smibert, P., and Satija, R. (2019). Comprehensive Integration of Single-Cell Data. Cell *177*, 1888–1902.e1821.

Subramanian, A., Tamayo, P., Mootha, V.K., Mukherjee, S., Ebert, B.L., Gillette, M.A., Paulovich, A., Pomeroy, S.L., Golub, T.R., Lander, E.S., and Mesirov, J.P. (2005). Gene set enrichment analysis: a knowledge-based approach for interpreting genome-wide expression profiles. Proc. Natl. Acad. Sci. USA *102*, 15545–15550.

Tang, Y., Liu, J., Zhang, D., Xu, Z., Ji, J., and Wen, C. (2020). Cytokine Storm in COVID-19: The Current Evidence and Treatment Strategies. Front. Immunol. *11*, 1708.

von Pawel, J., Schiller, J.H., Shepherd, F.A., Fields, S.Z., Kleisbauer, J.P., Chrysson, N.G., Stewart, D.J., Clark, P.I., Palmer, M.C., Depierre, A., et al. (1999). Topotecan versus cyclophosphamide, doxorubicin, and vincristine for the treatment of recurrent small-cell lung cancer. J. Clin. Oncol. *17*, 658–667.

WHO REACT (Rapid Evidence Appraisal for COVID-19 Therapies) Working Group, Sterne, J.A.C., Murthy, S., Diaz, J.V., Slutsky, A.S., Villar, J., Angus, D.C., Annane, D., Azevedo, L.C.P., Berwanger, O., et al. (2020). Association Between Administration of Systemic Corticosteroids and Mortality Among Critically Ill Patients With COVID-19: a Meta-analysis. JAMA *324*, 1330–1341.

Wingett, S., Ewels, P., Furlan-Magaril, M., Nagano, T., Schoenfelder, S., Fraser, P., and Andrews, S. (2015). HiCUP: pipeline for mapping and processing Hi-C data. F1000Res. *4*, 1310.

Winkler, E.S., Bailey, A.L., Kafai, N.M., Nair, S., McCune, B.T., Yu, J., Fox, J.M., Chen, R.E., Earnest, J.T., Keeler, S.P., et al. (2020). SARS-CoV-2 infection of human ACE2-transgenic mice causes severe lung inflammation and impaired function. Nat. Immunol. *21*, 1327–1335.

Wong, C.K., Lam, C.W., Wu, A.K., Ip, W.K., Lee, N.L., Chan, I.H., Lit, L.C., Hui, D.S., Chan, M.H., Chung, S.S., and Sung, J.J. (2004). Plasma inflammatory cytokines and chemokines in severe acute respiratory syndrome. Clin. Exp. Immunol. *136*, 95–103.

Yu, G., Wang, L.G., Han, Y., and He, Q.Y. (2012). clusterProfiler: an R package for comparing biological themes among gene clusters. OMICS *16*, 284–287.

Zabidi, M.A., Arnold, C.D., Schernhuber, K., Pagani, M., Rath, M., Frank, O., and Stark, A. (2015). Enhancer-core-promoter specificity separates developmental and housekeeping gene regulation. Nature *518*, 556–559.

Zhang, Y., Liu, T., Meyer, C.A., Eeckhoute, J., Johnson, D.S., Bernstein, B.E., Nusbaum, C., Myers, R.M., Brown, M., Li, W., and Liu, X.S. (2008). Model-based analysis of ChIP-Seq (MACS). Genome Biol. *9*, R137.

Zhou, F., Yu, T., Du, R., Fan, G., Liu, Y., Liu, Z., Xiang, J., Wang, Y., Song, B., Gu, X., et al. (2020a). Clinical course and risk factors for mortality of adult inpatients with COVID-19 in Wuhan, China: a retrospective cohort study. Lancet *395*, 1054–1062.

Zhou, Y., Fu, B., Zheng, X., Wang, D., Zhao, C., Qi, Y., Sun, R., Tian, Z., Xu, X., and Wei, H. (2020b). Pathogenic T-cells and inflammatory monocytes incite inflammatory storms in severe COVID-19 patients. Natl. Sci. Rev. *7*, 998–1002.

STAR★METHODS

KEY RESOURCES TABLE

REAGENT or RESOURCE	SOURCE	IDENTIFIER
Antibodies		
anti-H3K27ac	Abcam	Abcam Cat# ab4729, RRID:AB_2118291
anti-SARS-CoV-2 Nucleoprotein (NP)	Produced in house (Center for Therapeutic Antibody Development(CTAD))	Cat#: NP1C7C7
Recombinant Anti-Topoisomerase I antibody [EPR5375]	Abcam	Abcam Cat# ab109374, RRID:AB_10861978
beta-Tubulin (9F3) Rabbit mAb (HRP Conjugate)	Cell Signaling Technologies	Cell Signaling Technology Cat# 5346, RRID:AB_1950376
Dynabeads M-280 Sheep Anti-Rabbit IgG	Thermo fisher scientific	Thermo Fisher Scientific Cat# 11203D, RRID:AB_2783009
anti-rabbit Alexa fluor 488nM	Thermo fisher scientific	# A-11008, RRID:AB_143165
Bacterial and virus strains		
SARS-related coronavirus 2 (SARS-CoV-2), isolate USA-WA1/2020	BEI Resources	Sequence ID: NR-52281
SARS-related coronavirus 2 (SARS-CoV-2), isolate HKG/13_P2/2020	Isolated in Vero E6 cells from the nasopharynx aspirate and throat swab of a confirmed COVID-19 patient in Hong Kong	Sequence ID: MT835140
Chemicals, peptides, and recombinant proteins		
Topotecan-hydrochloride	Cayman Chemical Company	Cat#:14129
Remdesivir	MedKoo Biosciences Inc	Cat#:329511
SBE-β-CD	MedChemExpress	Cat#:HY-17031
DMSO	Sigma	Cat#:D4540-500ML
PEG300	MedChemExpress	Cat#:HY-Y0873
Corn oil	MedChemExpress	Cat#:HY-Y1888
Critical commercial assays		
NEBNext Ultra II DNA Library Prep Kit for Illumina	NEB	Cat#:E7645S
NEBNext Multiplex Oligos for Illumina (Index Primers Set 2)	NEB	Cat#:E7500S
NEBNext Multiplex Oligos for Illumina (Index Primers Set 1)	NEB	Cat#:E7335S
NextSeq 500/550 High Output Kit v2.5 (150 Cycles)	Illumina	Cat#:20024907
NEBNext Ultra II Directional RNA Library Prep Kit for Illumina	NEB	Cat#:E7760S
NEBNext rRNA Depletion Kit (Human/Mouse/Rat)	NEB	Cat#:E6310L
RNAClean XP	Beckman Coulter	Cat#:A63987
AMPure XP	Beckman Coulter	Cat#:A63881
Lipofectamine RNAiMAX Transfection Reagent	Thermo fisher scientific	Cat#:13778075
MyOne C1 streptavidin beads	Thermo fisher scientific	Cat#: 65001
biotin-14-dATP	Jena Bioscience	Cat#:NU-835-BIO14-S

(*Continued on next page*)

Continued

REAGENT or RESOURCE	SOURCE	IDENTIFIER
Qubit 1X dsDNA HS Assay Kit	Thermo fisher scientific	Cat#:Q33231
NucleoSpin RNA Plus kit	NucleoSpin RNA Plus kit	Cat#:740955
Deposited data		
RNA-seq (Hamster Infection)	This study	GEO:GSE162619
H3K27ac ChIP-Seq	This study	GEO: GSE167528
Hi-C (SARS-CoV-2)	This study	GEO:GSE162619
Promoter Capture Hi-C	This study	GEO: GSE164533
Hi-C (Influenza; H5N1 in HBTE)	This study	GEO: GSE113703
RNA-seq (siTOP1 in A549-ACE2)	This study	GEO: GSE162619
Single cell RNA-seq of Patient BALFs	Liao et al., 2020	GEO: GSE145926
Immunopathological profiles in lungs of lethal COVID-19	Nienhold et al., 2020	GEO: GSE151764
H3K27ac ChIP-Seq (Influenza; H5N1 in HBTE)	This study	GEO: GSE113702
CisBP database	Lambert et al., 2019	http://cisbp.ccbr.utoronto.ca
Experimental models: cell lines		
A549	ATCC	ATCC Cat# CRL-7909, RRID:CVCL_0023
THP-1	ATCC	ATCC Cat# TIB-202, RRID:CVCL_0006
Vero-E6	ATCC	ATCC Cat# CRL-1586, RRID:CVCL_0574
A549-ACE2	Icahn School of Medicine at Mount Sinai	Daniloski et al., 2021
Calu3	ATCC	ATCC Cat# HTB-55, RRID:CVCL_0609
Experimental models: organisms/strains		
Golden Syrian Hamster	Charles River / Laboratory Animal Unit, University of Hong Kong (HKU)	Charles River Cat #: Crl:LVG(SYR)
B6.Cg-Tg(K18-866 ACE2)2 Prlmn/J (K18-hACE2)	Jackson Laboratories	IMSR Cat# JAX:034860, RRID:IMSR_JAX:034860
Oligonucleotides		
ON-TARGETplus Non-targeting Control Pool	Horizon Discovery	D-001810-10-20
ON-TARGETplus Human TOP1 siRNA	Horizon Discovery	L-005278-00-0005
qPCR primers	This Study	STAR Methods
Software and algorithms		
fgsea	Korotkevich et al., 2019	https://bioconductor.org/packages/release/bioc/html/fgsea.html
DoubletFinder	McGinnis et al., 2019	https://github.com/chris-mcginnis-ucsf/DoubletFinder
Seurat	Stuart et al., 2019	https://satijalab.org/seurat/
DESeq2	Love et al., 2014	https://bioconductor.org/packages/release/bioc/html/DESeq2.html
ChIP-seq Analysis pipeline	This study	https://github.com/MarioPujato/NextGenAligner
bedtools	Quinlan and Hall, 2010	https://github.com/arq5x/bedtools2/releases
HOMER	Heinz et al., 2010	http://homer.ucsd.edu/homer/
STAR	Dobin et al., 2013	https://github.com/alexdobin/STAR
HiCUP	Wingett et al., 2015	https://www.bioinformatics.babraham.ac.uk/projects/hicup/
CHiCAGO	Cairns et al., 2016	https://bioconductor.org/packages/release/bioc/html/Chicago.html

(*Continued on next page*)

Continued

REAGENT or RESOURCE	SOURCE	IDENTIFIER
Graphpad Prism 8.0	Graphpad	NA
Cutadapt	Martin, 2011	https://cutadapt.readthedocs.io/en/stable/
Limma	Ritchie et al., 2015	https://bioconductor.org/packages/release/bioc/html/limma.html
clusterProfiler	Yu et al., 2012	https://bioconductor.org/packages/release/bioc/html/clusterProfiler.html

RESOURCE AVAILABILITY

Lead contact

Further information and requests for reagents may be directed to and will be fulfilled by Lead Contact Ivan Marazzi (ivan.marazzi@mssm.edu).

Materials availability

All unique/stable reagents generated in this study are available from the Lead Contact with a completed Materials Transfer Agreement.

Data and code availability

Next generation sequencing data are deposited on GEO. Hi-C/RNA-seq (SARS-CoV-2): GSE162619; Promoter Capture Hi-C: GSE164533; H3K27ac ChIP-seq: GSE167528; Hi-C (Influenza): GSE113703, H3K27ac ChIP-seq (Influenza): GSE113702.

EXPERIMENTAL MODEL AND SUBJECT DETAILS

Cells

Human alveolar basal epithelial carcinoma cells (A549, ATCC CCL-185), Calu-3 cells and monkey kidney epithelial cells (Vero E6, ATCC CRL-1586) were maintained at 37°C and 5% CO_2 and cultured in Dulbecco's Modified Eagle's Medium (DMEM; GIBCO) supplemented with 10% fetal bovine serum (FBS; GIBCO). THP-1 cells were cultured in RPMI supplemented with 10% FBS, 10 mM non-essential amino acids, 1 mM sodium pyruvate and 4 mM L-glutamine.

Viral strains

For infections in A549-ACE2 cells and K18-hACE2 mice, SARS-related coronavirus 2 (SARS-CoV-2), isolate USA-WA1/2020 (NR-52281) was used (Blanco-Melo et al., 2020; Daniloski et al., 2021). For Infections with THP-1 cells (Figure S3C) and hamsters in Figure 3, isolate HKG/13_P2/2020 (MT835140) was used. For Infections with hamsters in Figure S4 and all infections in K18-hACE2 mice (Figures 5 and S5), isolate USA-WA1/2020 (NR-52281) was used. SARS-CoV-2 was grown in Vero E6 cells in DMEM supplemented with 2% FBS, 4.5 g/L D-glucose, 4 mM L-glutamine, 10 mM non-essential amino acids, 1 mM sodium pyruvate and 10 mM HEPES. Plaque assays were used to determine infectious titers of SARS-CoV-2 by infection of Vero E6 cells in Minimum Essential Media supplemented with 2% FBS, 4 mM L-glutamine, 0.2% BSA, 10 mM HEPES and 0.12% NaHCO3 and 0.7% agar.

METHOD DETAILS

Generation of A549-ACE2 cells

Generation of A549-ACE2 cells was performed as previously described (Blanco-Melo et al., 2020; Daniloski et al., 2021). Briefly, A549 cells were transduced with lentiviral vector pHR-PGK expressing human ACE2 coding sequence. A549 cells were then transduced with the lentivirus in the presence of polybrene (8 μg/ml). Cells were used for downstream assays after 48h post transduction.

Preparation of siTOP1 sequencing libraries

7.5E4 A549-ACE2 cells were plated in a 24 well dishes. 16 hours post plating, cells were transfected with control, scrambled (siSCR), TOP1-targeting (siTOP1) or no siRNA (no siRNA) using Lipofectamine RNAiMax to a final concentration of 50nM. 48hours post transfection, the media was replaced, and fresh media was added to each well. Cells were then mock infected (PBS only) or infected with SARS-CoV-2 at MOI 0.5. Viral isolate USA-WA1/2020 (NR-52281) was used in these experiments. 24 hours post infection, media was removed, and cells were lysed in 250ul of Trizol reagent (Thermo Scientific). RNA was then extracted using the Purelink RNA Minikit (Invitrogen) with DNaseI treatment, according to the manufacturer's recommendations. RNA quality was determined using the RNA 6000 Nano kit and the Eukaryote Total RNA Nano assay on the Agilent 2100 Bioanalyzer System. RNA quantity was determined by Qubit RNA HS Assay Kit.

To then prepare RNA-sequencing libraries, 300 ng of RNA was depleted of ribosomal RNA using NEBNext® rRNA Depletion Kit (Human/Mouse/Rat), according to the manusfacturer's instructions. Libraries were then prepared from rRNA depleted RNA using the NEBNext® Ultra II Directional RNA Library Prep Kit for Illumina®, following the manufacturer's instructions. Final libraries were quantified and sizing was determined using the High Sensitivity DNA Assay reagents and chip in the Agilent 2100 Bioanalyzer System and the Qubit 1X dsDNA HS Assay Kit respectively. Individual libraries were then pooled and sequenced using 75bp paired end on the NextSeq 550 using the NextSeq 500/550 High Output Kit

ChIP-seq library preparation

To prepare ChIP-Sequencing libraries, ~2E5 A549-ACE2 cells were plated into 12 well dishes. Cells were either mock infected (PBS only) or infected with SARS-CoV-2 virus at MOI 0.5. Viral isolate USA-WA1/2020 (NR-52281) was used in these experiments. 24 hours post infection, media was removed from the well, and replaced with Fixation buffer (PBS, 2% FBS, 1% Methanol-Free Formaldehye). Cells were fixed at room temperature for 10 min. 2M Glycine was then added to a final concentration of 0.125M, and cells were incubated at room temperature for 5min to quench the reaction. Supernatants were removed from wells, and each well was washed 3 times with cold PBS. Cells were then lysed in the well using 250ul of SDS Lysis Buffer [100mM NaCl, 50mM Tris pH8.0, 5mM EDTA, 0.02% NaN3, 0.5% SDS + 1X Halt Protease and Phosphatase Inhibitor (Thermo Scientific)] and cell lysates were collected in a 1.5ml tube and snap frozen at −80°C. On the day of sonication, lysates were thawed, and diluted with 125ul of Triton Dilution Buffer [100mM Tris pH8.5, 100mM NaCl, 5mM EDTA, 0.02% NaN3, 5% Triton X-100 + 1X Halt Protease and Phosphatase Inhibitor]. Lysates were then sonicated for 5 - 30 s ON/ 30 s OFF cycles twice using the Bioruptor Pico. Each sonicated lysate was then precleared using 10ul of Rabbit-IgG Dynabeads for 1 hour, rotating at 4°C. 1ug of anti-H3K27ac antibody was then added to 300ul of pre-cleared lysate. Immunoprecipitation (IP) was performed with overnight rotation at 4°C. To recover IP-complexes, 10ul of Dynabeads M-280 Sheep anti-Rabbit IgG were added to each reaction and tubes were rotated for 2 hours at 4°C. Bead-chromatin complexes were then washed 6 times on a magnet using ice cold RIPA wash buffer [50mM HEPES-KOH pH7.6, 100mM LiCl, 1mM EDTA, 1% NP-40, 0.5% Na-Deoxycholate]. Washed beads were then incubated in 125ul Elution buffer [1% SDS, 0.1M NaHCO3] at 65°C overnight for elution and de-crosslinking. ChIP DNA was then purified using the MinElute PCR purification kit (QIAGEN) and quantified using the Qubit 1X dsDNA HS Assay Kit.

ChIP libraries were prepared using the NEBNext® Ultra II DNA Library Prep Kit for Illumina following the manufacturer's recommendations. 1ng of ChIP-DNA was used to prepare each library. ChIP input libraries were prepared by pooling equal amounts of purified sonicated and non-IPed DNA from each sample. 1ng of the pooled ChIP-input DNA was used for library preparation. Libraries were quantified and sizing was determined using the High Sensitivity DNA Assay reagents and chip in the Agilent 2100 Bioanalyzer System and the Qubit 1X dsDNA HS Assay Kit respectively. Individual libraries were then pooled and sequenced 75bp paired end on the NextSeq 550 using the NextSeq 500/550 High Output Kit v2.5.

Preparation of HiC libraries

In situ Hi-C was performed as described (Heinz et al., 2018) with modifications. The day before infection, 200k A549-ACE2 cells were plated in a 12 well dishes. Cells were either mock-infected (PBS only) or infected with SARS-CoV-2 virus at MOI 0.5. Viral isolate USA-WA1/2020 (NR-52281) was used in these experiments. Twenty-four hours post infection, media was removed from the well, and replaced with Fixation buffer (PBS, 2% FBS, 1% Methanol-Free Formaldehyde). Cells were fixed at room temperature for 10 min. 2M Glycine was then added to a final concentration of 0.125M, and cells were incubated at room temperature for 5min to quench the reaction. Supernatants were then removed wells, and each well was washed 2 times with cold PBS. Cells were then lysed in the well using 250 μl of Lysis Buffer [0.5% SDS + Halt Protease and Phosphatase Inhibitors (Thermo Scientific)]. Cell lysates were collected in a 1.5ml tube. 1.5 mU RNaseA (Thermo Scientific) was added to each lysate, and lysates were then incubated at 37oC for 1h. RNaseA treated lysates were then snap frozen and stored in −80°C. After thawing, nuclei were collected at 1500 g for 5 minutes at room temperature. Most of the supernatant was discarded, leaving the nuclei in 10 μl liquid. Samples were resuspended in reaction buffer (25 μl 10% Triton X-100, 25 μl 10x Dpn II buffer, 188 μl water) and rotated at 37°C, 8 RPM for 15 minutes. Chromatin was digested overnight (ON) with either 2 μl (100 U) Dpn II (NEB) (later experiments) at 37°C, rotating overhead with 8 RPM. Nuclei were collected by centrifugation at 1500 g for 5 minutes at room temperature, 225 μl of the supernatant were discarded, leaving the nuclei in 25 μl liquid, and overhangs were filled in with Biotin-14-dATP by adding 75 μl Klenow Master Mix (54.45 μl water, 7.5 μl NEBuffer 2, 0.35 μl 10 mM dCTP, 0.35 μl 10 mM dTTP, 0.35 μl 10 mM dGTP, 7.5 μl 0.4 mM Biotin-14-dATP (Invitrogen), 2 μl 10% Triton X-100, 2.5 μl (12.5 U) Klenow fragment (Enzymatics)) and rotating overhead at RT, 8 RPM for 40 minutes. Reactions were stopped by adding 2.5 μl 0.5 M EDTA and placed on ice. Proximity ligation was performed by transferring the entire reaction into 1.5 mL Eppendorf tubes containing 400 μl ligase mix (322.5 μl water, 40 μl 10x T4 DNA ligase buffer (Enzymatics), 36 μl 10% Triton X-100, 0.5 μl 10% BSA, 1 μl (600 U) T4 DNA ligase (HC, Enzymatics) and rotating ON at 16°C, 8 RPM. Reactions were stopped with 20 μl 0.5 M EDTA, treated with 1 μl 10 mg/ml DNase-free RNase A for 15 minutes at 42°C, then 31 μl 5 M NaCl, 29 μl 10% SDS and 5 μl 20 mg/ml DNase-free proteinase K (Thermo) were added, proteins digested for 1 h at 55°C while shaking at 800 RPM, then crosslinks reversed ON at 65°C. After extraction with 600 μl pH 8-buffered phenol/chloroform/isoamyl alcohol (Ambion) followed by extraction with 600 μl chloroform, DNA was precipitated with 1.5 μl (22.5 μg) Glycoblue (Ambion) and 1400 μl 100% ethanol ON at −20°C. After centrifugation for 20' at 16000 g, 4°C, the DNA pellet was washed twice with 80% ethanol, and the pellet air-dried and dissolved in 131 μl TT (0.05% Tween 20/Tris pH 8). DNA (200 ng) was sheared to 300 bp in 130 μl TT on a Covaris E220 sonicator using the manufacturer's protocol. Biotinylated DNA was captured on

Dynabeads MyOne Streptavidin T1 (Thermo) by combining the sonicated DNA sample (130 μl) with 20 μl Dynabeads that had previously been washed with 1x B&W buffer (2X B&W: 10 mM Tris-HCl pH = 7.5, 1 mM EDTA, 2 M NaCl) and had been resuspended in 130 μl 2x B&W containing 0.2% Tween 20. The binding reaction was rotated at RT for 45 minutes, and DNA-bound beads were vigorously washed twice with 150 μl 1x B&W/0.1% Triton X-100, once with 180 μl TET (0.05% Tween 20, 10 mM Tris pH 8, 1 mM EDTA). Libraries were prepared on-beads using an NEBnext Ultra II DNA library prep kit using half the reagent/reaction volumes given in NEB's instruction manual and 1.6 pmol Bioo DNA sequencing adapters (Illumina TruSeq-compatible) per reaction. Reactions were stopped by adding 5 μl 0.5 M EDTA, beads collected on a magnet and washed twice with 150 μl 1x B&W/0.1% Triton X-100, twice with 180 μl TET and resuspended in 20 μl TT (0.05% Tween 20, 10 mM Tris pH 8.0). Libraries were amplified by PCR for 10 cycles (98°C, 30 s; 10x [98°C, 10 s; 63°C, 20 s; 72°C, 30 s]; 72°C, 2 min; 4°C, ∞), using 10 μl of the bead suspension in a 50 μl reaction with NEBNext Ultra II Q5 2x master mix (NEB) and 0.5 μM each Solexa 1GA/1GB primers (Solexa 1GA: AATGATACGGCGACCACCGA, Solexa 1GB: CAAGCAGAAGA CGGCATACGA). Libraries were precipitated onto magnetic beads by adding 40 μl 20% PEG8000/2.5 M NaCl and 2 μl SpeedBeads (8.9% PEG final) to 48 μl PCR reaction, thorough mixing by vortexing followed by 10-minute incubation at RT. Beads were collected using a magnet and the supernatant discarded. After washing beads twice by adding 180 μl 80% EtOH, moving the tube strip 6x from side to side of the magnet, collecting beads and discarding the supernatant, beads were air-dried, and DNA eluted by adding 20 μl TT. Libraries were sequenced paired-end for 42 cycles each to a depth of approximately 250 million reads per experiment on an Illumina NextSeq 500 sequencer.

Preparation of hamster RNA sequencing libraries

For RNA sequencing analyses in infected hamsters shown in Figure 3, infected hamsters that were treated with TPT or vehicle control, were euthanized at days 4 and 6 post infection. Uninfected hamsters were used as controls. After euthanasia, lung left inferior lobe from hamsters were cut into pieces and lysed with RA1 lysis buffer provided with the *NucleoSpin® RNA Plus* kit (Macherey-nagel), RNA extraction was performed according the manufacturer's recommendations, including an on-column genomic DNA digestion step. RNA sequencing library preparation and sequencing were then performed by BGI Genomics

Hamster infections

For experiments shown in Figure 3, Female Golden Syrian hamster, aged 6-8 week old (~70-100 g), were obtained from Laboratory Animal Unit, University of Hong Kong (HKU). All experiments were performed in a Biosafety Level-3 animal facility, LKS Facility of Medicine, HKU. The study has been approved by the Committee on the Use of Live Animals in Teaching and Research, HKU. Virus stock (isolate HKG/13_P2/2020 (MT835140)) was diluted with Phosphate-buffered saline (PBS) to 2 × 104 PFU/ml. Syrian hamsters were obtained from the LASEC, Chinese University of Hong Kong via the Centre for Comparative Medicine Research at the University of Hong Kong. Hamsters were anesthetized with ketamine (150mg/kg) and xylazine (10 mg/mg) and then intranasally inoculation with 50 ul of diluted viruses containing 10^3 PFU of viruses. For drug treatments, 10mg/kg TPT resuspended in vehicle [5% DMSO + 5% corn oil in PBS] or vehicle alone was administered intraperitoneally to animals on the indicated days post infection.

For experiments shown in Figure S4, infection procedures were performed following protocols approved by the Icahn School of Medicine at Mount Sinai Institutional Animal Care and Use Committee (IACUC). Animal studies were carried out in strict accordance with the recommendations in the Guide for the Care and Use of Laboratory Animals of the National Research Council. 7-10 week old (~120-140 g) female Golden Syrian hamsters (Charles River) were anesthetized using 90mg/kg Ketamine and 2mg/kg Xylazine by intraperitoneal injection. Once anesthetized, hamsters were intransally infected with 1E5 PFU of SARS-CoV-2 virus (isolate USA-WA1/2020 (NR-52281)) re-suspended in 100ul of PBS. Animals were monitored daily for clinical signs of illness and weight loss after infection. For drug treatments, 2mg/kg TPT resuspended in vehicle [4.5% DMSO + 20% Sulfobutylether-β-Cyclodextrin (SBE-β-CD) in PBS] or vehicle alone was administered intraperitoneally to animals on the indicated days post infection.

K18-hACE2 mice infections

All mice infection procedures were performed following protocols approved by the Icahn School of Medicine at Mount Sinai Institutional Animal Care and Use Committee (IACUC). Animal studies were carried out in strict accordance with the recommendations in the Guide for the Care and Use of Laboratory Animals of the National Research Council. 5-10 week old female B6.Cg-Tg(K18-ACE2) 2Prlmn/J (K18-hACE2) mice purchased from Jackson Laboratories (Bar Harbor, ME) were anesthetized by an intraperitoneal injection of 90mg/kg Ketamine and 2 mg/kg xylazine. Once anesthetized, mice were infected with 1E4 PFU of SARS-CoV-2 virus (isolate USA-WA1/2020 (NR-52281)) suspended in 30ul of PBS. Mice were monitored daily for clinical signs of illness and weight loss after infection. Animals that reached 80% bodyweight or clinical signs that are irrevocably linked with death were humanely euthanized by intraperitoneal injection of 60mg/kg pentobarbital.

For drug treatments, 2mg/kg Topotecan-hydrochloride (TPT; 14129, Cayman Chemical Company) re-suspended in vehicle [4.5% DMSO + 20% Sulfobutylether-β-Cyclodextrin (SBE-β-CD) in PBS] was administered intraperitoneally to animals on the indicated days post infection.

Extraction of RNA from lungs of infected hamsters and mice

Upon euthanasia, the superior lobe of infected hACE2-KI mice or Golden Syrian hamsters were collected for RNA extraction. Lungs were lysed and homogenized in Trizol. RNA extraction was performed using the Purelink RNA Mini Kit with a DNaseI treatment step,

according to the manufacturer's recommendations. cDNA was synthesized from RNA using the High-Capacity cDNA Reverse Transcription Kit (ThermoFisher).

Histological analysis

For histological slides shown in Figures 3E–3H, Lung left superior lobes of infected Golden Syrian hamster were fixed in 4% paraformaldehyde and then processed for paraffin embedding. The 4μm tissue sections were stained with hematoxylin and eosin for histopathological examination. Images were with Olympus BX53 semi-motorized fluorescence microscope using cellSens imaging software.

For histological slides shown in Figures S4D and S4E, the left lung lobe of infected Golden Syrian hamsters was fixed in 10% formalin for 48 hours. Embedding in paraffin blocks and staining with H&E were conducted by the Biorepository and Pathology Dean's CoRE at the the Icahn School of Medicine at Mount Sinai. Microscopic sections were analyzed in a blinded fashion by the same pathologist (A.M.). A number was randomly assigned by the investigator to discriminate each section, which was then submitted for analysis. No information about treatments and mouse genotypes was communicated to the pathologist. Lungs were scored by the area involved in broncho-pneumonia.

Promoter capture Hi-C (PCHi-C)

We combined PCHi-C (Schoenfelder et al., 2015) with Hi-C library generation as described previously (Nagano et al., 2017), with some modifications. Cells were fixed in 2% PFA for 10 minutes, lysed in lysis buffer (30 minutes on ice), and digested with *DpnII* (NEB) overnight at 37C rotating (950rpm). Restriction overhangs were filled-in with Klenow (NEB) using biotin-14-dATP (Jena Bioscience), and ligation was performed in ligation buffer for 4 hours at 16C (T4 DNA ligase; Life Technologies). After overnight decrosslinking at 65C, the ligated DNA was tagmented to produce fragments of 300-700 bp range. Ligation products were isolated using MyOne C1 streptavidin beads (Life Technologies), followed by washing with Wash&Binding buffer and nuclease-free water. Isolated Hi-C ligation products on the beads were then used directly for PCR amplification, and the final Hi-C library was purified with AMPure XP beads (Beckman Coulter). Promoter Capture Hi-C was performed using a custom-design Agilent SureSelect system following the manufacturer's protocol.

Quantification of viral titers by plaque assays

For quantification of viral titers in the lungs tissues of infected animals, the middle, inferior and post-caval lobes of infected mice/hamsters were collected and homogenized in 1ml of ice-cold PBS. Lysates were then centrifuged at 10000rpm for 5min to remove cellular debris, and the cleared lysates transferred to new tubes. Lysates were then diluted in 10-fold dilutions 6 times. Quantification of infectious SARS-CoV-2 titers was then performed by plaque assays. Briefly, Vero-E6 cells were plated as confluent monolayers in 12 well dishes. Media was removed, and wells washed in 1ml of PBS. 200ul of diluted lysates was then added per well and allowed to incubate for 1 hour at 37°C. After viral adsorption, lysates were removed from the well and cells were overlaid with Minimum Essential Media supplemented with 2% FBS, 4 mM L-glutamine, 0.2% BSA, 10 mM HEPES and 0.12% NaHCO3 and 0.7% agar. 72h post infection, agar plugs were fixed in 10% formalin for 24h before being removed. Plaques were visualized by immune staining with anti-mouse SARS-CoV-2 Nucleoprotein antibodies (mAb 1C7) for 1 hour at RTP followed by anti-mouse HRP-conjugated secondary antibody (abcam) for 1 hour at RTP after 3 washes in PBS + 0.1% Tween 20. Plaques were then developed using the TrueBlue substrate (KPL-Seracare) and viral titers calculated and expressed as PFU/ml

Quantification of neutralizing antibodies in serum (microneutralization assays)

Microneutralization assays were performed as previously described (Amanat et al., 2020). Briefly, Vero E6 cells were seeded at a density of 20,000 cells per well in a 96-well cell culture plate in complete Dulbecco's Modified Eagle Medium (cDMEM). The following day, heat-inactivated serum samples (dilution of 1:10) were serially diluted threefold in 1 × MEM (10% 10 × minimal essential medium (GIBCO), 2 mM L-glutamine, 0.1% sodium bicarbonate (wt/vol; GIBCO), 10 mM 4-(2-hydroxyethyl)-1-piperazineethanesulfonic acid (HEPES; GIBCO), 100 U ml–1 penicillin, 100 ug/ml–1 streptomycin (GIBCO) and 0.2% bovine serum albumin (MP Biomedicals)). Then, 80 μl of each serum dilution and 80 μl of the SARS-CoV-2 virus, diluted to a concentration of 100 TCID50 (50% tissue culture infectious dose) were added to a 96-well cell culture plate and allowed to incubate for 1 h at room temperature. Media was then removed from the Vero E6 cells, and 120ul of the virus-serum mixture added to each well. The plate was then incubated at 37 °C for 1 h. Virus-serum mixture was then removed from the cells, and 100ul of each corresponding serum dilution and 100ul of 1X MEM/1%FBS added back to each well. Cells were incubated for 48h at 37 °C before being fixed with 10% paraformaldehyde for 24h at 4°C. After fixation, formaldehyde was removed, and cells were washed with 200ul PBS, before being permeabilized with 150ul PBS/0.1% Triton X-100 for 15min. Plates were then washed three times with PBS + 0.1% Tween 20 (PBST) and blocked in 3% Milk/PBST for 1h at RTP. 100ul of 1:1000 diluted mAb 1C7 iwas then added to each well. Plates were incubated for a further 1h at RTP. After incubation, plates were wash 3 times with PBST, before anti-mouse IgG-HRP (1:3000 in 3% milk) was added to the well. Plates were incubated for a further 1 hour at RTP, before being washed 3 times with PBST. Finally, SIGMAFAST OPD (Sigma-Aldrich) was added to wells. The reaction was stopped after 10 min through the addition of 50ul 3M HCl. OD490 was then measured on a Synergy 4 plate reader (BioTek). Concentrations of antibodies in serum were blank normalized and curve-fitted to calculate IC_{50} using Graphpad prism 8.0.

TPT treatment of SARS-CoV-2 infected A549-ACE2 cells

1E5 A549-ACE2 cells were plated in a 24 well dishes 16h prior to infection. For infection, cells were then mock infected (PBS only) or infected with SARS-CoV-2 at MOI 2. TPT was added to a final concentration of 100nM or 500nM. DMSO controls were also included. 8 and 24 hours post infection, media was removed, and cells were lysed in 250ul of Trizol reagent (Thermo Scientific). Uninfected and drug treated cells were also infected as controls. RNA was then extracted using the Purelink RNA Minikit (Invitrogen) with DNaseI treatment, according to the manufacturer's recommendations. Viral isolate USA-WA1/2020 (NR-52281) was used in these experiments.

TPT treatment of THP1 cells

THP1 cells were plated in 48 well dishes. For purified viral RNA (vRNA) treatment, THP1 cells were transfected with 1ug purified SARS-CoV-2 (isolate HKG/13_P2/2020 (MT835140)) vRNA using Lipofectamine 3000 according to the manufacturer's recommendations. For supernatant treated cells, media of THP1 cells was replaced with conditioned media from infected cells. At 6 hours post treatment (either by vRNA transfection or conditioned media), remaining media was removed from THP1 cells, and cells were lysed in Trizol. RNA was then extracted according to the manufacturer's recommendations. To make conditioned media, Calu-3 cells were infected with 0.1 MOI SAR-CoV-2 (HKG/13_P2/2020 (MT835140)). At 72hpi, supernatant was collected and filtered using YM100 Amicon Ultra Filter to remove residual viruses. Filtered supernatants were then used for downstream assays.

Viral growth and cytotoxicity assays in the presence of TPT or Remdesivir

Experiments were performed as previously described (Gordon et al., 2020). Briefly, 24h hours prior to the assay, 2000 Vero-E6 cells were seeded in 96 well plates and incubated at 37 °C, 5% CO2.Medium was replaced 2 hours before infection with DMEM (2% FBS) media containing drugs of interest at different doses and at concentrations 50% greater than those indicated. Cells were then infected with 100 PFU (MOI = 0.025) SARS-CoV-2 (isolate USA-WA1/2020 (NR-52281)) in 50ul, bringing the final drug concentration to those indicated. Plates were then incubated for 48h at 37 °C, 5% CO2. Supernatants were then removed and cells were fixed in 4% paraformaldehyde for 24h. To determine % of infected cells, cells were stained for NP protein (1° antibody: anti-sera produced in the García -Sastre laboratory; 1:10,000; 2° antibody: anti-rabbit Alexa flour 488nM) and a DAPI counterstain. Infected cells were visualized and quantified using the Celigo (Nexcelcom) imaging cytometer. Accumulation of viral NP protein in the nucleus was used as a proxy for infectivity. The percentage of infected cells per well was quantified as ((infected cells/total cells) − background) × 100 and the DMSO control was then set to 100% infection for analysis. The IC_{50} was then determined using Graphpad Prism 8.0 software by performing a non linear regression (inhibitor versus response) curve fit. To measure cytotoxicity of drugs, MTT assays (Roche) were performed according to the manufacturer's instructions. These assays were performed in uninfected Vero-E6 cells using the same concentrations of drugs, and performed concurrently with viral replication assays. All assays were performed in biologically independent triplicates.

QUANTIFICATION AND STATISTICAL ANALYSIS

Mouse infection studies

Mice were randomly assigned into treatment groups. Statistical significance between survival curves was calculated using a Log-rank (Mantel-Cox) test using Graphpad Prism 8.0 software. Differences in weight loss curves were determined using a Two-Way Mixed Model ANOVA in Graphpad Prism 8.0 Software. Data are shown as ± SEM. To determine effects of drug treatment on morbidity, the maximum weight lost for each mouse in each condition was tabulated, Mice were grouped by those that had a maximum weight loss of either > 15% or ≤ 15%. Differences in percentages of mice falling in these two groups under late TPT treatment or DMSO vehicle control treatment was then calculated using a Fisher's Exact Test in Graphpad Prism 8.0 software.

Quantitative qPCR assays

The following primers were used for qPCR: [Human] HPRT1 F: TGCTGAGGATTTGGAAAGGG, HPRT1 R: ACAGAGGGCTACAATGTGATG, *CXCL8* F: ATACTCCAAACCTTTCCACCC, *CXCL8* R: TCTGCACCCAGTTTTCCTTG, *CXCL3* F: AAGTGTGAATGTAAGGTCCCC, *CXCL3* R: GTGCTCCCCTTGTTCAGTATC, *CXCL2* F: AACCGAAGTCATAGCCACAC, *CXCL2* R: CTTCTGGTCAGTTGGATTTGC, *IL6* F: ACTCACCTCTTCAGAACGAATTG, *IL6* R: CCATCTTTGGAAGGTTCAGGTTG, *TNFAIP3* F: GATAGAAATCCCCGTCCAAGG, *TNFAIP3* R: CTGCCATTTCTTGTACTCATGC, *EGR1* F: TGTCACCAACTCCTTCAGC, *EGR1* R: TCCTGTCCTTTAAGTCTCTTGTG, *CXCL10* F: *CXCL10* R *CXCL11* F *CXCL11* R: [Mouse] *Hprt* F: GGCCAGACTTTGTTGGATTTG, *Hprt* R: CGCTCATCTTAGGCTTTGTATTTG *Ccr8* F: AGTGGGCAGCTCTGAAAC, *Ccr8* R: GCTCCATCGTGTAATCCATCG, *Il10* F: AGCCGGGAAGACAATAACTG, *Il10* R: GGAGTCGGTTAGCAGTATGTTG, *Arg1* F: AAGAATGGAAGAGTCAGTGTGG, *Arg1* R: GGGAGTGTTGATGTCAGTGTG, *Ccr2* F: GCTCTACATTCACTCCTTCCAC, *Ccr2* R: ACCACTGTCTTTGAGGCTTG, *Ccl5* F: GGGTACCATGAAGATCTCTGC, *Ccl5* R: TCTAGGGAGAGGTAGGCAAAG, *Ccr5* F: TCCAGCAAGACAATCCTGATC, *Ccr5* R: AACCATTCCTACTCCCAAGC [Hamster] *Tbp* F: CCCTTGTACCCTTCACCTATG, *Tbp* R: ACATCCAAGATTCACCGTGG, *Ccl5* F: GCAAGGAAAGCAAATGGAGAC, *Ccl5* R: GTGCTGGTTTCTTGGGTTTG, *Ccr5* F: GACATCTACCTGCTCAACCTG, *Ccr5* R: AACCAATGTGATAGAGCCCTG, *Ccr1* F: CTCCTTCTCAGAGTTGTCACAG, *Ccr1* R: GCACAAGACACAGAACACAAG, *Ccl4* F: TCCTGACCAGAAAAGGCAAG, *Ccl4* R: AGCTCAGTTCAACTCCAAGTC. qPCR assays performed for the quantification of gene expression in the *in vitro* models were done in 3 biological replicates.

Expression of genes of interest were normalized to that of a housekeeping gene using the comparative Cq method, where using the comparative Cq method: $2^{-\Delta Cq}$, where ΔCq = Cq Target gene - Cq Housekeeping gene. For human samples either HPRT1 or ACTB was used as a housekeeping gene. For mouse and hamster samples, Hprt and Tbp were used respectively. Where samples were normalized to mock infected samples, ΔCq of infected replicates were exponentially transformed to $2^{-\Delta Cq}$ before being averaged and the standard deviation determined. The mean of infected samples was then compared to that of the corresponding uninfected (mock treated samples), such that the final ratio of $\Delta Cq^{Infected}$ / $\Delta Cq^{Uninfected}$ was determined. This method takes into account effects associated with experimental treatment. Statistical significance in gene expression was estimated with Graphpad Prism 8.0 software, and determined using two-tailed Student's t test under the assumption of equal variances between groups. Data are shown as ± SD.

qPCR assays performed for gene expression analysis in the lungs of infected animals were done with 3-4 biological replicates (3-4 infected animals/condition). Expression of genes of interest were normalized to that of a housekeeping gene using the comparative Cq method, where using the relative Cq method: $2^{-\Delta Cq}$, where ΔCq = Cq Target gene - Cq Housekeeping gene. Statistical significance in gene expression was estimated with Graphpad Prism 8.0 software, and determined using one or two-tailed Student's t test under the assumption of equal variances between groups. Tests used are indicated in the legends. Data are shown as ± SEM.

Illumina short read RNA sequencing analyses

After adaptor removal with cutadapt (Martin, 2011) and base-quality trimming to remove 3′read sequences if more than 20 bases with Q < 20 were present, paired-end reads were mapped to the SARS-CoV-2 and human (hg38) or hamster (*Mesocricetus auratus*; MesAur1.0) reference genomes with STAR . Gene-count summaries were generated with featureCounts (Liao et al., 2014). A numeric matrix of raw read counts was generated, with genes in rows and samples in columns, and used for differential gene expression analysis with the Bioconductor Limma package (Ritchie et al., 2015) after removing genes with less than 50 total reads across all samples or of less than 200 nucleotides in length. Normalization factors were computed on the filtered data matrix using the weighted trimmed mean of M-values (TMM) method, followed by voom (Law et al., 2014) mean-variance transformation in preparation for Limma linear modeling. To specifically identify the effect of siRNA mediated TOP1 depletion on the inflammatory responses to SARS-CoV-2 in A549-ACE2 cells shown in Figure 2, we used interaction model (siTOP1_Infected:siTOP_uninfected - siSCR_Infected:siSCR_uninfected or no_siRNA_infected:no_siRNA:uninfected - siSCR_Infected:siSCR_uninfected), that takes into account basal differences between conditions. Gene ontology analysis were performed with clusterProfiler (Yu et al., 2012). To identify TPT dependent gene expression changes in infected hamsters showin in Figure 3, we performed pairwise contrast between experimental groups (i.e: TPT D4 – DMSO D4; TPT D6 – DMSO D6). Pairwise comparisons were then performed between treatment groups and eBayes adjusted P values were corrected for multiple testing using the Benjamin-Hochberg (BH) method and used to select genes with significant expression differences (fold change > 1.5, adjusted P value < 0.05). For gene ontology analysis in hamsters, hamster gene ids were converted to available human orthologs using ENSEMBL, and inputted into clusterProfiler (Yu et al., 2012) program in R.

GSEA analysis for gene signatures in TPT treated hamsters

We identified TOP1 inhibitor gene signatures from TPT-treated Syrian hamsters infected with SARS-CoV-2. We defined the up- and downregulated signatures as genes differentially expressed after 4 or 6 days of treatment (log2|FC| > 1, FDR = 10%). We converted hamster genes to available human orthologs using ENSEMBL (Release 101). We downloaded normalized transcript expression from targeted RNA-seq (398 genes) on lung autopsy tissue from COVID19 patients (16 patients, 34 samples), normal lung tissue (6 patients, 17 samples), and lung tissue from from bacterial or viral pneumonia (4 patients, 5 samples) (Nienhold et al., 2020; GEO accession: GSE151764). Gene set enrichment analysis (Subramanian et al., 2005) was performed using the R package fgsea (Korotkevich et al., 2019). We used Tukey's multiple comparison test to identify significant differences in mean normalized enrichment scores.

For gene set enrichment analysis of lung-cell-type gene, we downloaded UMI counts of single-cell RNA-seq of bronchoalveolar lavage fluid (BALF) from patients with moderate and severe COVID19, along with healthy controls (Liao et al., 2020). We removed a sample from a patient with severe COVID19 identified to be co-infected with HPMV (Bost et al., 2020). We removed cell doublets from individual patient samples using DoubletFinder (McGinnis et al., 2019). We integrated patient samples using canonical correlation analysis in Seurat (Stuart et al., 2019).

We aggregated UMI counts for each cell-type from each patient sample, keeping "pseudo-bulk" samples mad up of at least 10 cells. Pseudo-bulk counts were robustly normalized with DESeq2 (Love et al., 2014)and gene expression was Z-scored across cells. We performed GSEA (Subramanian et al., 2005) using the R package fgsea (Korotkevich et al., 2019).

ChIP-seq analysis

ChIP-seq datasets were processed and analyzed using an in-house automated pipeline (https://github.com/MarioPujato/NextGenAligner). Briefly, basic quality control for raw sequencing reads was performed using FASTQC (version 0.11.2) (https://www.bioinformatics.babraham.ac.uk/projects/fastqc). Adaptor sequences were removed using Trim Galore (version 0.4.2) (https://www.bioinformatics.babraham.ac.uk/projects/trim_galore/), a wrapper script that

runs cutadapt (version 1.9.1) to remove the detected adaptor sequence from the reads. The quality-controlled reads were aligned to the reference human genome (hg19/GRCh37) using bowtie2 (version 2.3.4.1) (Langmead and Salzberg, 2012). Aligned reads were then sorted using samtools (version 1.8) (Li et al., 2009) and duplicate reads were removed using picard (version 1.89)

(https://broadinstitute.github.io/picard/). Peaks were called using MACS2 (version 2.1.0) (https://github.com/macs3-project/MACS) (Zhang et al., 2008) with the control/input aligned reads as background (callpeak -g hs -q 0.01 –broad -c input/control). ENCODE blacklist regions (Amemiya et al., 2019) were removed using the hg19-blacklist.v2.bed.gz file available at https://github.com/Boyle-Lab/Blacklist/tree/master/lists.

The ChIP-seq experimental design consisted of triplicates experiments for each condition (0hr, 8hr, 24hr infections). PCA analysis indicating strong agreement between experimental replicates and clear separation between conditions (Figure S1A) Sequencing reads from replicates were thus combined, and alignment and peak calling was again performed as described above. For differential peak analysis, the union set of all peaks from these three conditions was generated using bedtools (Quinlan and Hall, 2010). For each of the resulting genomic regions, read counts were obtained for all 9 replicates. These read counts used as input to DESeq2 (Love et al., 2014). A fold change cutoff of greater than or equal to 1.5 and an FDR-corrected p value cutoff of less than or equal to 0.05 were used to identify differential peaks for each pairwise comparison between conditions.

We used the HOMER suite of tools (Heinz et al., 2010), modified to use a log base two scoring system and to include the large set of human motifs contained in the CisBP database (build 2.0) (Lambert et al., 2019) to identify enriched motifs within the sequences of differential and shared ChIP-seq peaks. To minimize redundancy, motifs were grouped into classes using the following procedure. Each human transcription factor was assigned the single best p value obtained for any of its corresponding motifs. Transcription factors with identical best motifs were merged then into a single class.

HiC analysis

Hi-C data was processed as described in Heinz et al. (2018). Briefly, Hi-C reads were trimmed at MboI/DpnII recognition sites (GATC) and aligned to the human genome (GRCh38/hg38) using STAR (Dobin et al., 2013), keeping only read pairs that both map to unique genomic locations for further analysis (MAPQ > 10). All PCR duplicates were also removed. PCA analysis of Hi-C experiments used to define chromatin compartments were performed with HOMER (Lin et al., 2012). For each chromosome, a balanced and distance normalized contact matrix was generated using window size of 50 kb sampled every 25 kb, reporting the ratios of observed to expected contact frequencies for any two regions. The correlation coefficient of the interaction profiles for any two regions across the entire chromosome were then calculated to generate a correlation matrix (also visualized in Figure 1A). This matrix was then analyzed using Principal Component Analysis (PCA) from the prcomp function in R (https://www.r-project.org), and the eigenvector loadings for each 25 kb region along the first principal component were assigned to each region (PC1 values). The PC1 values from each chromosome were scaled by their standard deviation to make them more comparable across chromosomes and analysis parameters. For each chromosome, PC1 values are multiplied by −1 if negative PC1 regions are more strongly enriched for active chromatin regions defined by H3K27ac peaks to ensure the positive PC1 values align with the A/permissive compartment (as opposed to the B/inert compartment). chrY was excluded from the PCA analysis due to its small size and high repeat content. Balanced, normalized Hi-C contact maps were generated at 25 kb resolution for visualization (Figure 1A). Assignment of PC1 values to Gencode gene promoters and other features was performed using HOMER's annotatePeaks.pl function using the results from the PCA analysis.

Promoter capture Hi-C analysis

Sequencing data from three biological replicates of PCHi-C at each of the three time points were aligned and quality-controlled with HiCUP (Wingett et al., 2015). *DpnII* fragment-level reads were pooled over consecutive fragments over the total length of at least 5k, except for the baited promoter fragments that were left unbinned. To achieve a balanced dataset for the analysis of promoter interaction dynamics across time points, sequencing data for each replicate were subsampled to a similar number of HiCUP-processed valid captured reads per time point. Significant interactions were then detected for each time point jointly across the replicates by CHiCAGO (Cairns et al., 2016), with minNPerBait set to 90 and all other parameters left at defaults.

A peak matrix was generated listing the CHiCAGO scores at each time point for all interactions that exceeded a CHiCAGO score cutoff of 5 in at least one time point. K-means clustering was used to partition the peak matrix into 7 clusters based on arcsinh-transformed CHiCAGO scores, corresponding to interactions detected in a single time point (“0h,” “8h,” “24h”), two time points (“0+8hpi,” “0+24hpi,” “8+24hpi”) or all time points (“0+8+24hpi”). To minimize the impact of false-negative calls at each time point on cluster assignment, we additionally called interactions in each full-sized single replicate and filtered the above clusters to remove interactions that had CHiCAGO scores above 3 in any single replicate/time point, for which the corresponding cluster was negative (e.g., interactions in the 0hpi cluster were filtered out if they had scores > 3 in any of the single-replicate 8hpi or 24hpi calls, etc.). This filtered interaction set was then curated based on their k-means cluster assignment into three categories: lost (“0hpi” and “0+8h”), retained (the “0+8+24hpi” cluster) and gained (“8+24hpi” and “24hpi”), respectively, upon infection.

To assess the relationship between H3K27ac dynamics and changes in promoter-enhancer interactions at 0 versus 24 hpi, we used Fisher's test on 3x3 contingency tables between the “lost” (log2FC < −2; padj < 0.05), “constant” (padj > 0.1; baseMean > 50) and “gained” (log2FC > 2; padj < 0.05) H3K27ac peaks and the promoter interaction categories defined as above. Interactions without H3K27ac ChIP peaks at PIRs at either 0 or 24 hpi were removed from the analysis. Results were presented as heatmaps, with each combination of expression and promoter interaction category color-coded by the log-odds ratio (LORs) for the given versus the other two expression and promoter interaction categories combined, respectively. Confidence intervals (CIs) for the LORs were computed based on Fisher's exact test, with LORs whose CIs cross zero greyed out on the heatmaps.

To assess the relationship between gene expression dynamics and change in the number of connected active enhancers, we used the same promoter interaction and H3K27ac dynamics categories, and additionally classified genes into "down" (log2FC < 1, padj < 0.05), "neutral" (|log2FC < 0.5|, padj > 0.2) and "up" (log2FC > 1, padj < 0.05) at 24 versus 0 hpi. For each gene, change in the number of connected active enhancers *C* was computed as follows:

C = #(retained interactions with gained H3K27ac peaks) +
#(gained interactions with gained H3K27ac peaks) +
#(gained interactions with constant H3K27ac peaks) –
#(retained interactions with lost H3K27ac peaks) –
#(lost interactions with lost H3K27ac peaks) –
#(lost interactions with constant H3K27ac peaks).

Genes were partitioned into three categories based on this quantity: "reduced" ($C < 0$), "constant" ($C = 0$), "increased" ($C > 0$). The relationship between these categories and the gene expression category ("down," "neutral," "up") was probed and visualized using 3x3 contingency tables in the same manner as above.

Supplemental figures

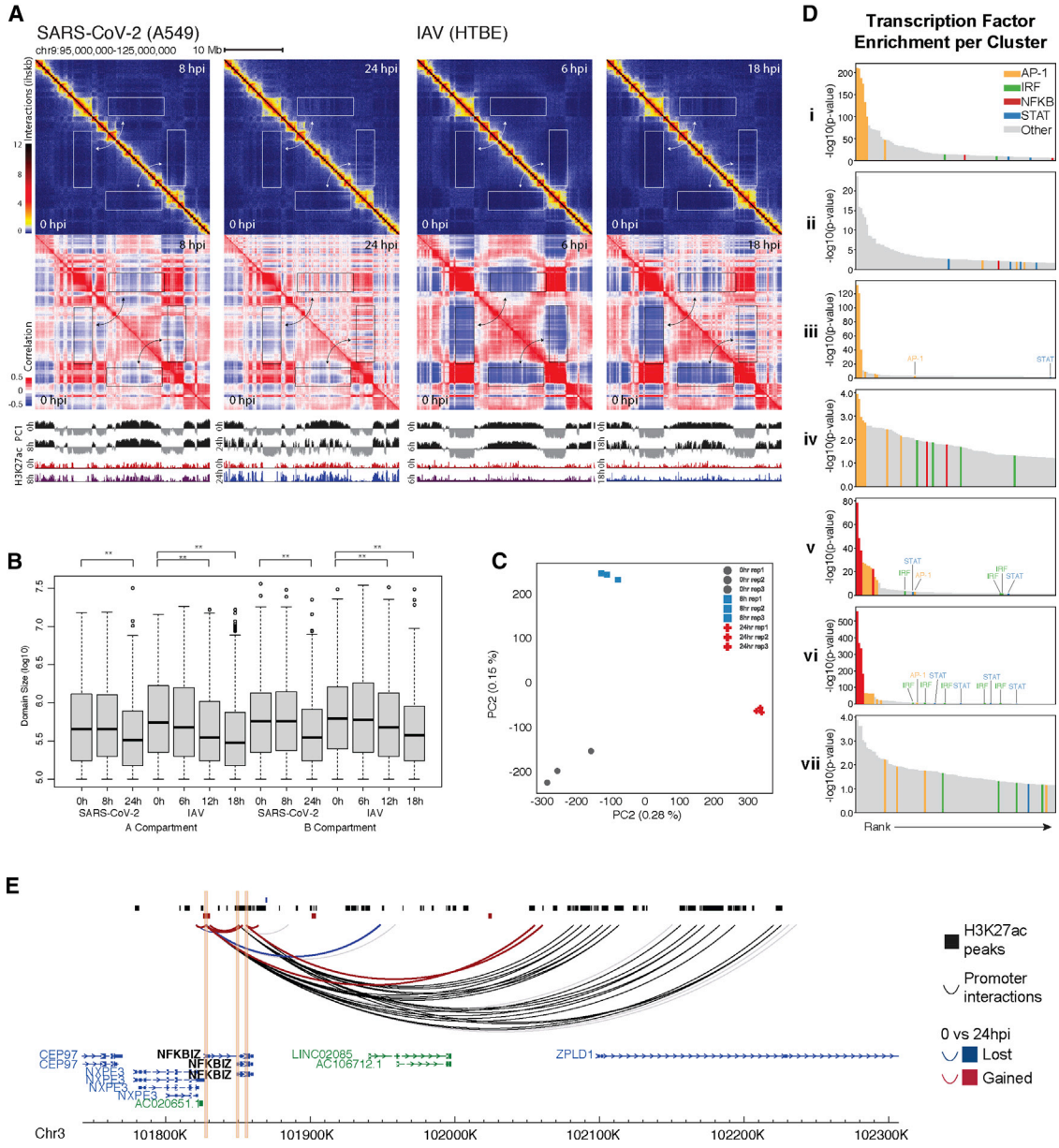

Figure S1. H3K27ac profiles in SARS-CoV-2-infected A549-ACE2 cells, related to Figure 1

(A) Upper panels: Normalized Hi-C contact matrices are shown for the uninfected (0hpi) control versus 8 hours (8 hpi; leftmost panel) or 24 hours post infection with SARS-CoV-2 (24 hpi; middle left panels) for a representative 30 Mb region of chromosome 9. Normalized Hi-C contact matrices for the same chromosome is shown in Influenza A (IAV) infected and control HBTE cells in the middle-right (0hpi versus 6hpi) and right most panels (0hpi versus 18hpi). White rectangles highlight regions with strong changes in interaction patterns between conditions. Middle panels: pairwise correlation matrices for comparisons shown in the upper panel. Lower panel: PC1 values, which represent the PCA loadings describing the chromatin compartment membership (+ values for the A compartment, - values for the B compartment) are shown along with H3K27ac ChIP-seq levels for the region depicted. Cells infected for 24 hours show increased segregation of chromatin into smaller A and B compartment domains in both Influenza A and SARS-CoV-2 infected cells.

(B) Distribution of A and B compartment domain sizes genome wide for uninfected control A549-ACE2 or HBTE cells, SARS-CoV-2 infected A549-ACE2 cells and IAV infected HBTE cells at the indicated time points.

(legend continued on next page)

(C) Principle Component (PCA) analysis of ChIP-seq experimental replicates. PCA was performed across the genome using the set of peaks identified in each experimental replicate. Percentage of variance expained by the first two components is shown along the axes. PCA was performed using scikit-learn (Pedregosa et al., 2011).

(D) Transcription factor binding site motif enrichment for each of the clusters shown in Figures 1C and 1D. Motif enrichment was calculated within H3K27ac-marked regions. Bar plots indicate the negative log p value of enrichment for the top 100 motif classes (see Methods). Bars are colored by motif. AP-1: Yellow; IRF: Green; NFKB: Red; STAT: Blue; Other: Grey

(E) Dynamics of promoter interactions and enhancer activity (proxied by K27ac) between 0 and 24 hpi for the *NFKBIZ* gene that is upregulated upon infection. K27ac peaks gained at 24hpi are highlighted in dark red (log_2-fold change (LFC) > 2, padj < 0.05); there were no lost H3K27ac peaks detected in this locus at the same level of stringency. *NFKBIZ* promoter interactions with K27ac regions ("enhancers") are shown as colored arcs, with lost and gained interactions at 24 hpi highlighted in blue and dark-red, respectively, and the rest shown in black. Light-gray arcs represent interactions with regions without K27ac detected at any time point.

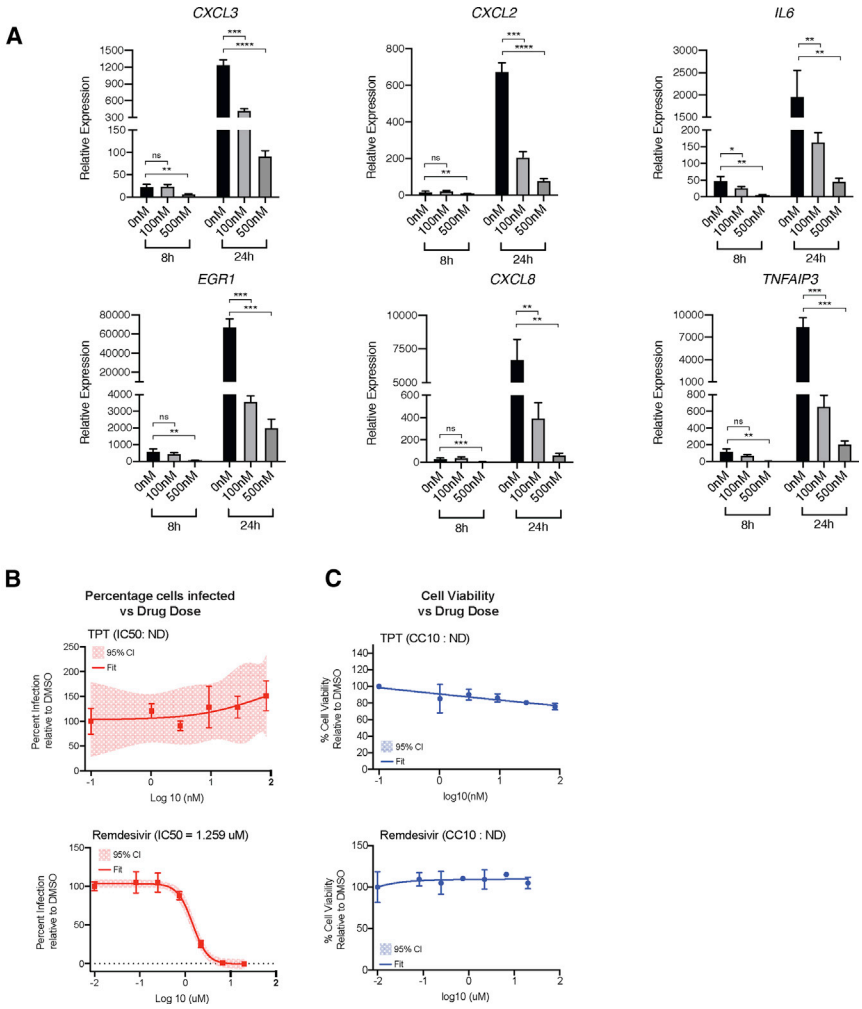

Figure S2. TPT treatment phenocopies siRNA-mediated TOP1 depletion in SARS-CoV-2-infected A549-ACE2 cells, related to Figure 2

(A) qPCR analysis of CXCL3, CXCL2, IL6, EGR1, CXCL8 and TNFAIP3 expression levels in the presence and absence of 0nM, 100nM or 500nM TPT at 8 or 24h post infection. Data are shown relative to the corresponding uninfected controls. Bars show the mean and standard deviation of 3 replicates. *$p < 0.05$, **$p < 0.01$, ***$p < 0.001$, ****$p < 0.0001$, ns: not significant by a two tailed Student's t test.

(B) Percentage of Vero-E6 cells infected with SARS-CoV-2 48h post infection and in the presence of the indicated concentration of TPT or Remdesivir. Shown are the mean and standard deviation of two independent replicates. Values shown are relative to DMSO (no drug) treated samples. Pink highlighted area shows the 95% confidence interval of the fitted curve (non-linear 4 parameter inhibitor versus response).

(C) Cell proliferation assays of Vero-E6 cells treated with the indicated concentrations of TPT or Remdesivir. Shown are the mean and standard deviation of two independent replicates. Values shown are relative to DMSO (no drug) treated samples. 95% confidence intervals (CI) could not be determined for the fitted curve (non-linear 4 parameter inhibitor versus response)

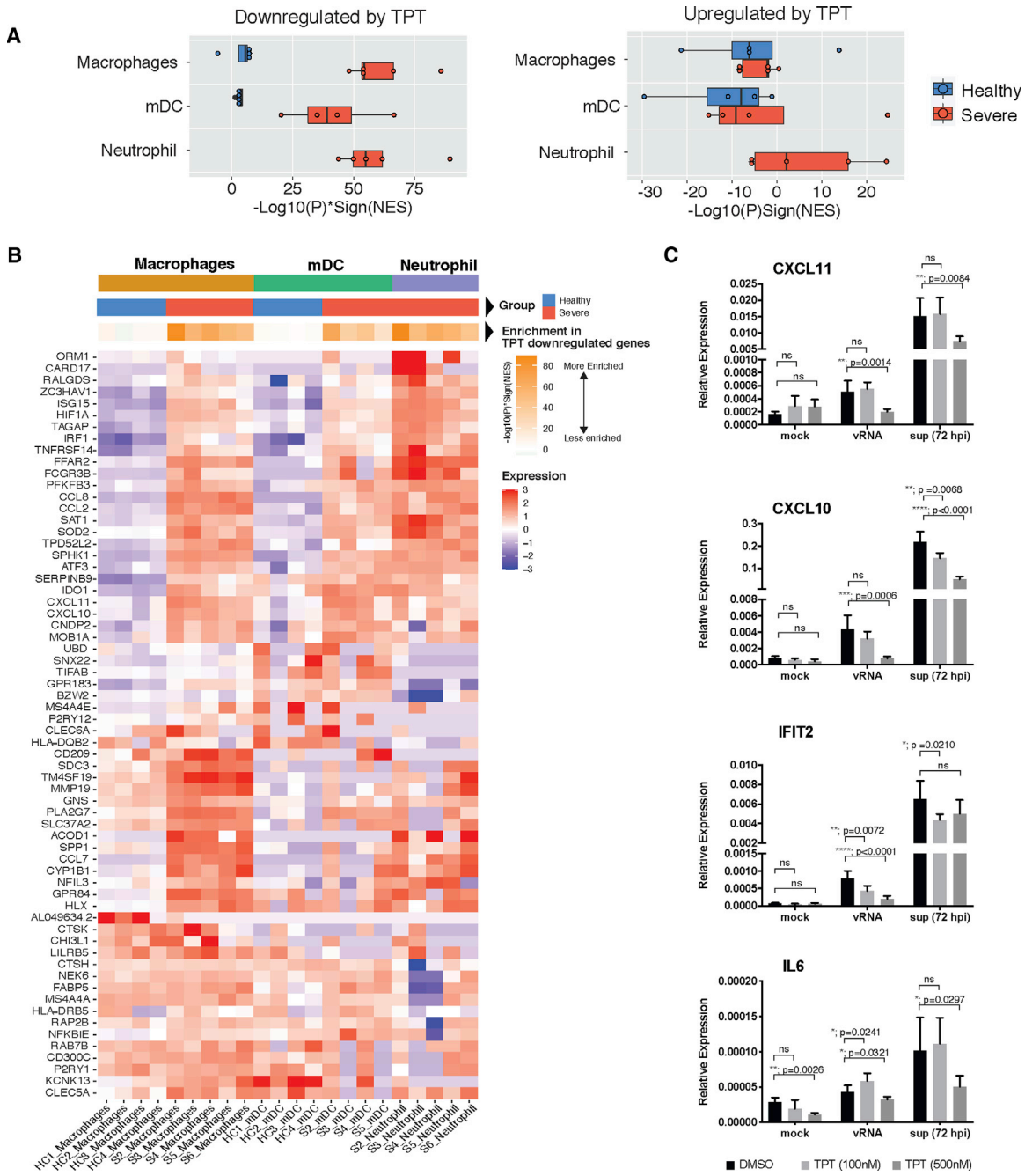

Figure S3. TPT suppresses gene programs in immune cell subsets, related to Figure 3

(A) Gene set enrichment analysis of lung-cell-type gene expression profiles from bronchoalveolar lavage fluid (BALF) of COVID19 patients with moderate and severe disease versus healthy patients (Liao et al., 2020). Signed –log10 adjusted P values indicate enrichment of downregulated (left panel) and upregulated (right panel) gene signatures from TPT-treated hamsters infected with SARS-CoV-2. The sign of enrichment is given by the normalized enrichment score (NES). (B) Expression by lung immune-cell type (macrophage, dendritic cells or neutrophils) of severe COVID19 patients and healthy controls (Liao et al., 2020) of genes downregulated in TPT-treated Sars-CoV-2-infected hamsters (log2|FC| > 1, FDR = 10%). Cell types are indicated by the topmost bar and in the column names; Macrophages: Orange, myeloid Dendritic cells (mDC): Green and Neutrophils: Purple. Patient groups are indicated by the second bar, where healthy patients are in blue, and severe COVID19 patiends in red. Gene set enrichment scores, calculated as −log10(P)*sign(NES) are indicated in the middle bar. The sign of enrichment is given by the normalized enrichment score (NES). Positive, higher scores indicate that TPT-inhibited genes are more upregulated in a given patient, whereas negative, lower scores indicate that TPT-inhibited genes are more downregulated in a given patient. The lower heatmap shows the individual gene expression profile of the indicated TPT-inhibited gene for a given patient (in columns). Heatmap columns are sorted by cell type and enrichment score from the highest (left) to lowest enrichment score (right).

(legend continued on next page)

(C) THP1 cells were transfected with purified SARS-CoV-2 viral RNA (vRNA) or treated with filtered, virus-free conditioned media supernatants from SARS-CoV infected Calu-3 cells (see STAR Methods) in the presence or absence of 100nM or 500nM of TPT. Expression of TOP1-dependent inflammatory genes were then measured by qPCR analysis. Data shown are mean and standard deviation of 4-6 biological replicates per condition. *$p < 0.05$; **$p < 0.01$, ***$p < 0.001$, ****$p < 0.0001$ by two tailed Student's T Test. Data are plotted relative to Actin B expression.

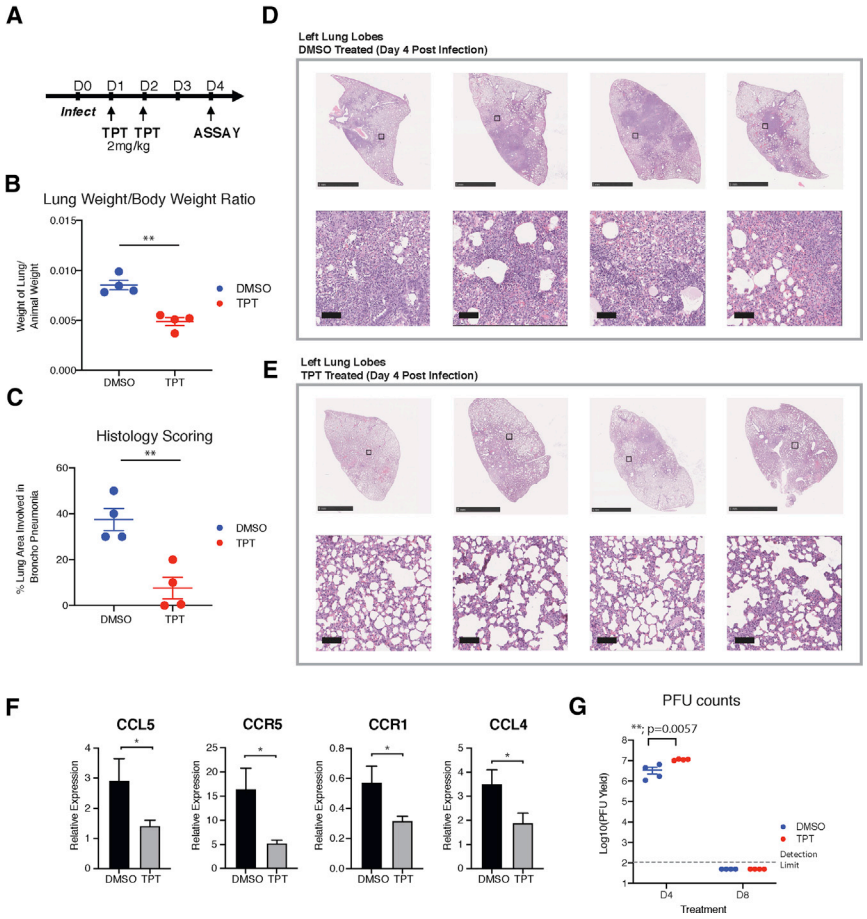

Figure S4. Reduced TPT dosages have similar beneficial effects in SARS-CoV-2-infected hamsters, related to Figure 3

(A) Schematic showing infection and treatment regime in 7-10 week old hamsters.

(B) Lung weight to body weight ratios of Hamsters infected with 1E4 PFU SARS-CoV-2 at Day 4 post infection, and treated with either DMSO (red) or 2mg/kg TPT (blue). Each dot represents an individual animal, and lines indicate the mean and SEM of Lung/Body weight ratios.

(C) Scatterplots depicting the percent of lung area that is involved in Broncho Pneumonia, as blindly scored by the pathologist (A.M). Each dot represents an individual animal, and the lines indicate the mean and SEM.

(D,E) Representative H&E sections of the left lung lobe of infected hamsters at day 4 post infection, and treated either with DMSO (D) or 2mg/kg TPT (E) . Scale bar: 5mm and 250uM for the upper and lower panels respectively

(F) Inflammatory gene expression in DMSO or TPT infected hamsters at day 4 post infection. Bars show the mean and SEM of 4 animals. *$p < 0.05$ by a one tailed Student's t test, assuming equal variances. Data are plotted relative to *Tbp* expression.

(G) Plaque assays were performed on lysates derived from the lungs of hamsters infected with 1E5 PFU of SARS-CoV-2 and treated with either DMSO vehicle control or 2mg/kg TPT. Lungs were isolated at Days 4 or 8 post infection. Each point represents one animal (n = 4/condition). Shown are the mean and SEM of the Log10(PFU yield/mL). p values were calculated using a two-tailed Student's t test. DL: Detection limit

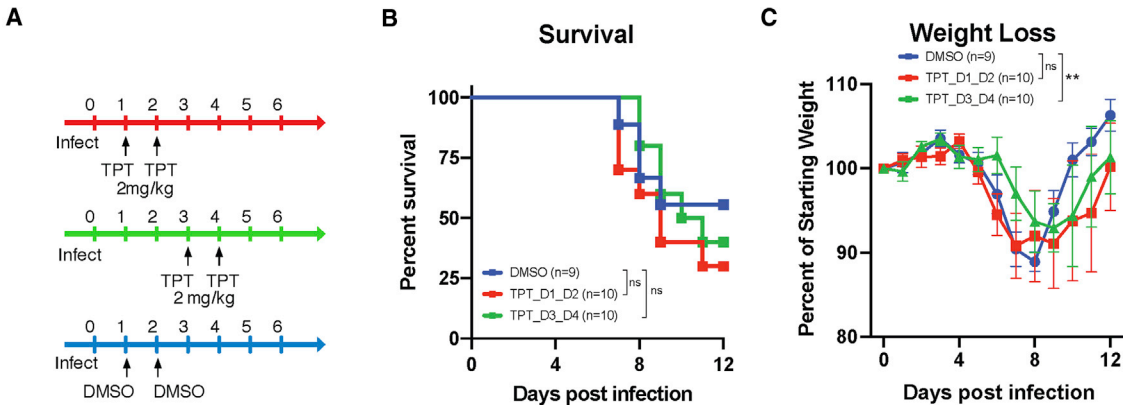

Figure S5. Late treatment of TPT in K18-hACE2 mice overs no survival benefit during SARS-CoV-2 infection, related to Figure 5

(A) Schematic showing infection and treatment regime in mice. Groups are color coded by treatment regime. Viral isolate USA-WA1/2020 (NR-52281) was used in these experiments.

(B) Survival curve of K18-hACE2 mice infected with 1E4 PFU of SARS-CoV-2 and subsequently subjected to the indicated TPT treatment regimes. Number of mice used are indicated in the legend. Blue: DMSO vehicle control only (n = 9); Red: TPT 2mg/kg on Days 1 and 2 post infection (n = 10); Green: TPT 2mg/kg on Days 3 and 4 post infection (n = 10). Ns: not significant, by logrank Mantel-Cox test.

(C) Weight loss curves in surviving mice shown in B. Numbers of mice at the end and start (end/start) points of the experiment are indicated in the legend keys. Weights are shown as means of the percentage of starting weights. Error bars show the SEM of each group. Blue: DMSO only; Red: TPT 2mg/kg on Days 1 and 2 post infection; Green: TPT 2mg/kg on Days 3 and 4 post infection; Purple: TPT 2mg/kg on Days 4 and 5 post infection. **$p < 0.01$; ns:not significant, by two-way mixed model ANOVA analysis.